ARTICLE

Check for updates

Photovoltaic retinal prosthesis restores high-resolution responses to single-pixel stimulation in blind retinas

Naïg Aurelia Ludmilla Chenais[1], Marta Jole Ildelfonsa Airaghi Leccardi [1] & Diego Ghezzi [1✉]

Retinal prostheses hold the promise of restoring vision in totally blind people. However, a decade of clinical trials highlighted quantitative limitations hampering the possibility of reaching this goal. A key challenge in retinal stimulation is to independently activate retinal neurons over a large portion of the subject's visual field. Reaching such a goal would significantly improve the perception accuracy in retinal implants' users, along with their spatial cognition, attention, ambient mapping and interaction with the environment. Here we show a wide-field, high-density and high-resolution photovoltaic epiretinal prosthesis for artificial vision (POLYRETINA). The prosthesis embeds 10,498 physically and functionally independent photovoltaic pixels, allowing for wide retinal coverage and high-resolution stimulation. Single-pixel illumination reproducibly induced network-mediated responses from retinal ganglion cells at safe irradiance levels. Furthermore, POLYRETINA allowed response discrimination with a high spatial resolution equivalent to the pixel pitch (120 μm) thanks to the network-mediated stimulation mechanism. This approach could allow mid-peripheral artificial vision in patients with retinitis pigmentosa.

[1] Medtronic Chair in Neuroengineering, Center for Neuroprosthetics and Institute of Bioengineering, School of Engineering, École Polytechnique fédérale de Lausanne, Chemin des Mines 9, Geneva, Switzerland. ✉email: diego.ghezzi@epfl.ch

Visual prostheses provide artificial vision through electrical stimulation of the preserved neurons in the visual system[1–3]. Over the years, several devices were proposed, including retinal, optic nerve and cortical implants[4–9]. Still, so far, only retinal prostheses have reached large testing in patients together with tremendous improvements from the technological perspective[10–13].

Retinal implants have been predominantly tested in blind patients affected by retinitis pigmentosa, a set of inherited retinal dystrophies causing the progressive loss of retinal photoreceptors, the visual field's constriction and eventually blindness[14]. Retinitis pigmentosa has a prevalence of ~1:4000 individuals, although totally blind people are rare (i.e., with no remaining light perception). Retinitis pigmentosa patients implanted with either epiretinal or subretinal prostheses could localise and identify letters or objects, and perform orientation tasks[15–17]. Nevertheless, despite the research community's effort and the patients' enthusiasm, most of the latter ceased using their implant in the first to the third year following their surgery[18]. Furthermore, one-third of the users of the Argus® II epiretinal prosthesis (the most implanted so far) declared that the device had a neutral impact on their quality of life after three years[19].

This discouragement can be attributed to quantitative limitations in artificial vision provided by retinal implants[18]. Retinal prostheses approved by regulatory agencies provide at best a visual angle of 20° (Argus® II[4]), and despite already being an incredible achievement in medical technology, such angle does not allow for safe and independent navigation in open spaces with obstacles and moving objects[20,21]. Independent mobility is of primary importance to increase the quality of life in profoundly blind patients with retinitis pigmentosa[22]. In addition, the coarse visual resolution offered by the device (i.e., for the Argus® II[4], 6 × 10 electrodes with a 525-μm pitch), combined with the small visual angle, provides little help in daily tasks involving object identification and recognition. Last, patients reported that retinal prostheses are cognitively exhausting due to the constant need for space decomposition[18]: because of the limited visual angle, the users are instructed to move their head and body to scan the environment. Scanning implies a constant visual decomposition and mental reconstruction of the visual scene, often guided by a complex pairing of the coarse visual information with audio-tactile cues[18]. Studies under simulated prosthetic vision identified a visual angle of 30° as the minimal requirement to efficiently complete everyday mobility and manipulation tasks[23–27]. However, this number might underestimate the real needs of implanted patients, which exhibit poor performance in those tasks, due to the perceptual and behavioural learning required to adapt to the spatially fractioned artificial vision[28,29]. The small visual angle is a significant bottleneck preventing patients affected by retinitis pigmentosa from efficiently performing daily activities. New retinal prostheses should overcome this challenge and restore a large enough visual angle fitting the natural scanning via eye movements to provide a helpful and valuable visual aid to patients with retinitis pigmentosa. Wide-field retinal prostheses enabling theoretical visual angles larger than 30° were recently proposed and tested in preclinical studies to meet these requirements[11,30].

Nevertheless, the visual angle is not the only barrier. Object identification and recognition require devices able to provide enough resolution. Wide-field arrays were so far designed for epiretinal placement only since large subretinal implants might encounter considerable difficulty in the surgical placement and represent a high risk of retinal detachment[31–33]. However, clinical trials showed that the best visual resolution was achieved using subretinal prostheses. The highest visual acuities reported to date, as measured with the Landolt-C test, were 20/460 (logMAR 1.37) with the subretinal implant PRIMA[34] and 20/546 (logMAR 1.43) with the subretinal implant Alpha-AMS[35]. Grating acuities reported in the literature range from 20/1260 with the epiretinal Argus® II implant[36] to 20/364 with the subretinal Alpha-AMS implant[37]. The inadequate performance of epiretinal prostheses like the Argus® II can be attributed to two factors: on the one hand, the implantable pulse generator, the transscleral cable and the feedlines in the array strongly limit the number and density of the electrodes, despite the large retinal coverage allowed by the epiretinal placement. On the other hand, the nerve fibre's direct activation distorts the retinotopic map by activating the axon of cells far from the electrode.

Here, we propose a wide-field curved organic photovoltaic epiretinal prosthesis with a high pixel density to address the aforementioned limitations. The high-density POLYRETINA implant was conceived to offer a large visual angle requiring minimal head scanning and a high resolution through epiretinal network-mediated stimulation, thus overcoming the nerve fibre's direct activation. However, a high pixel density of the prosthesis does not necessarily correlate with high visual discrimination since the response resolution at the retinal ganglion cell (RGC) level might be altered by the high spatial interconnectivity of the retinal network[33,38,39]. Therefore, we investigated ex vivo the response resolution provided by this high-density retinal prosthesis. Our results demonstrated that POLYRETINA could achieve a high spatial resolution in epiretinal stimulation, which is a substantial step forward for artificial vision.

Results

High-density retinal prosthesis. POLYRETINA is a wide-field high-density epiretinal prosthesis that contains 10,498 photovoltaic pixels (80-μm diameter, 120-μm pitch) distributed over an active area of 13 mm in diameter with a density of 79.1 pixels mm^{-2} (Fig. 1a, b). Once bonded to its curved flexible support, the active area is slightly stretched to 13.4 mm, and the prosthesis covers a visual angle of ~43° (750 mrad). Compared to the first POLYRETINA design[11], the number of pixels and their density were increased, together with two other technical improvements. First, titanium (Ti) electrodes were coated with a titanium nitride (TiN) layer to enhance the stimulation efficiency while keeping a safe capacitive stimulation. Second, the polymer-based layers below each cathode were patterned to generate physically independent photovoltaic pixels (Fig. 1c) and avoid cracks between rigid platforms made out of SU-8 (Fig. 1b).

The fabrication of a high-density array brings on several challenges. First, the higher the pixel density, the higher the risk that the pixels would crack during the device's hemispherical shaping. We performed finite element analysis simulations to estimate the level of tensile stress and strain occurring onto the cathodes during hemispherical shaping (Fig. 1d, e). The TiN coating reduced the tensile strain from −0.55 (Ti pixels) to −0.13% (TiN-coated pixels) and the tensile stress from 574.8 (Ti) to 310.9 MPa (TiN). The reduction of tensile stress during hemispherical shaping further protects the metal cathodes (Fig. 1b).

Second, a higher pixel density might induce crosstalk during stimulation with neighbouring pixels. To rule out this possibility, we measured the radial voltage spreading (Fig. 2a) in three directions (D1, D2 and D3 in Fig. 2b) using a glass microelectrode upon single-pixel pulsed illumination (560 nm, 10 ms). The minimum irradiance level required to activate RGCs ex vivo is ~100 of μW mm^{-2} for large-field illumination[11]; yet, to exclude crosstalk even at very high irradiance levels, we performed the experiment at 22.65 mW mm^{-2}, the maximal irradiance attainable by the illumination system. For each direction, the voltage
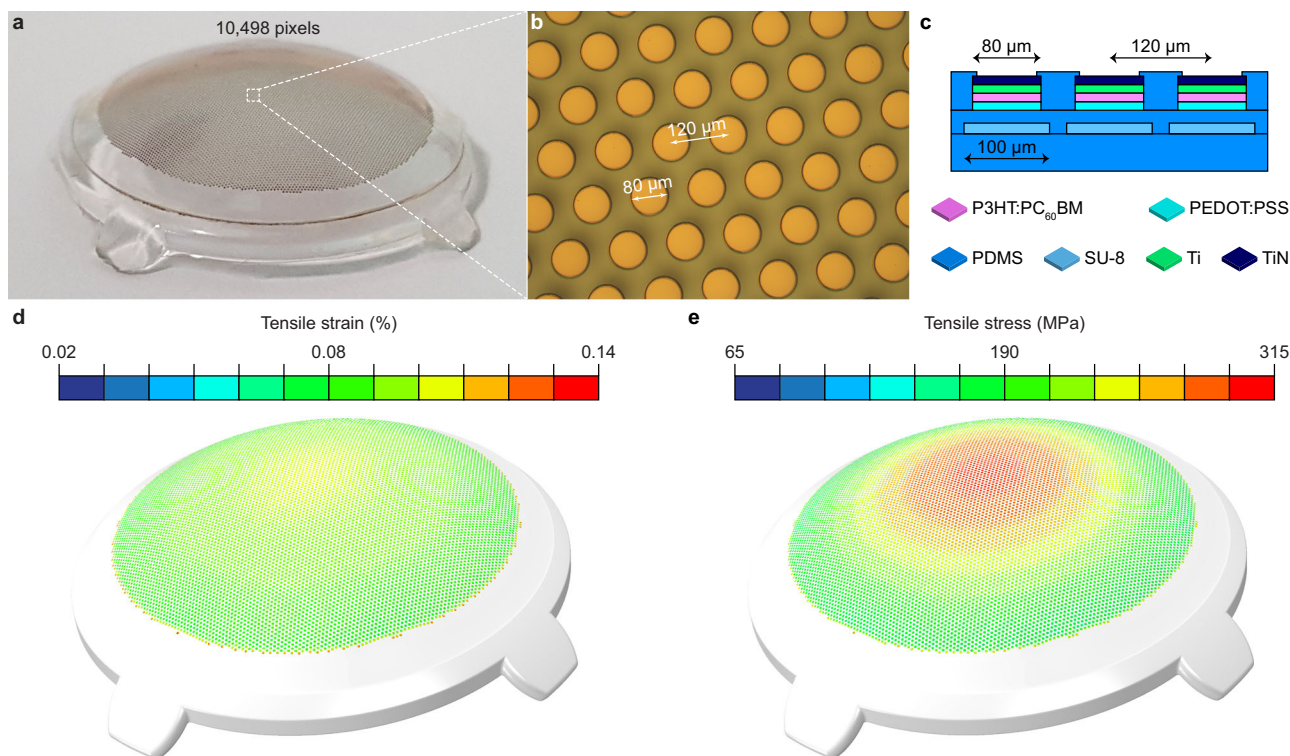
Fig. 1 High-density POLYRETINA device. a Picture of the high-density POLYRETINA prosthesis with 10,498 photovoltaic pixels. **b** Magnified view of the 80-μm diameter and 120-μm pitch photovoltaic pixels. **c** Sketch of the cross-section structure of the POLYRETINA photovoltaic interface before bonding to the hemispherical dome. The layer's thicknesses are as follow base PDMS layer: 50 μm; SU-8 platforms: 6 μm; second PDMS layer embedding SU-8 platforms: 15 μm; PEDOT:PSS: 50 nm, P3HT:PCBM: 100 nm, Ti-TiN: 80–60 nm, final PDMS layer: 4 μm. PDMS polydimethylsiloxane, PEDOT poly(3,4-ethylenedioxythiophene), PSS poly(styrenesulfonate), P3HT regioregular poly(3-hexylthiophene-2,5-diyl), PC60BM [6,6]-phenyl-C61-butyric acid methyl ester, Ti titanium, TiN titanium nitride. **d** Tensile strain simulated at the level of TiN. **e** Tensile stress simulated at the level of TiN.

generated from the pixel was measured in several points at increasing distance from the illuminated pixel (red points in Fig. 2b) and interpolated in a two-dimensional colour map (Fig. 2c). The voltage generated by single-pixel illumination remained localised above the pixel. In order to ensure that neighbouring pixels do not induce crosstalk, we repeated the experiment activating one pixel (Fig. 2d, left), one pixel with one surrounding corona of pixels (seven pixels; Fig. 2d, middle left), one pixel with two surrounding coronas of pixels (nineteen pixels; Fig. 2d, middle right), or the two surrounding coronas of pixels with the central pixel off (eighteen pixels; Fig. 2d, right). For each condition, the normalised voltage profiles in the three principal directions were averaged. The average plot of the voltage profile showed that the voltage generated by each pixel is sharply discriminated from one of the neighbouring pixels and does not show a voltage summation effect, in all the configurations tested (Fig. 2e). Even in the extreme case where the central pixel is off while the surrounding eighteen pixels are on, there is very high contrast in the voltage drop between the central pixel and the neighbouring ones (Fig. 2e, right), although a small residual potential is present also onto the central pixel. These results showed that the pixels are electrically independent (i.e., no crosstalk). However, it must be noted that the voltage measures were taken close to the device's surface (2–5 μm distance). Such sharp discrimination of the voltage profile might be reduced at larger distances from the array, where RGCs and bipolar cells (BCs) are located.

Third, high-density retinal prostheses would represent a useful advancement only if stimulation of RGCs can be achieved by single-pixel illumination. Thus, TiN was coated on top of the pixels to increase their stimulation efficiency. Using Kelvin Probe

Force Microscopy (KPFM), we evaluated the changes in the surface potential generated at the cathode upon illumination (560 nm, 60 s, 0.9 mW mm^{-2}) with and without TiN coating (Fig. 3a). The irradiance level was set to 0.9 mW mm^{-2} since our previous results showed a saturation of the RGC response beyond this value[11]. TiN-coated pixels led to a statistically significant higher change in the surface potential compared to Ti pixels (Fig. 3b; $P = 0.0083$, two-tailed unpaired t test). Next, we measured the photo-current (PC) and the photovoltage (PV) generated by the pixels upon illumination (565 nm, 10 ms) at increasing irradiance levels. We fabricated chips embedding six pixels, each of them connected to a contact pad to measure the signal at the cathode against a platinum reference electrode immersed in saline solution (Fig. 3c). The mean PC density (PCD) and PV were both higher for TiN-coated pixels upon illumination at increasing irradiance levels (Fig. 3f, g). We further evaluated the PCD and the PV at the representative irradiance level of 0.9 mW mm^{-2} (Fig. 3h): a statistically significant difference between Ti and TiN-coated pixels was found for both the PCD ($P = 0.0288$, two-tailed unpaired t test) and the PV ($P < 0.0001$, two-tailed unpaired t test). The surface area of the cathodes was measured with an atomic force microscope (AFM) over an area of 500×500 nm^2 (Fig. 3i, j). On average ($n = 3$ pixels), TiN-coated pixels showed a statistically higher surface area compared to Ti pixels ($P = 0.0024$, two-tailed unpaired t test).

These results confirmed that the photovoltaic pixels are physically and functionally independent. The coating with TiN reduced the mechanical stress of the pixels and increased their photovoltaic performance by likely reducing the electrode–electrolyte impedance, increasing the interface capacitance and reducing the parasitic resistances of the photovoltaic
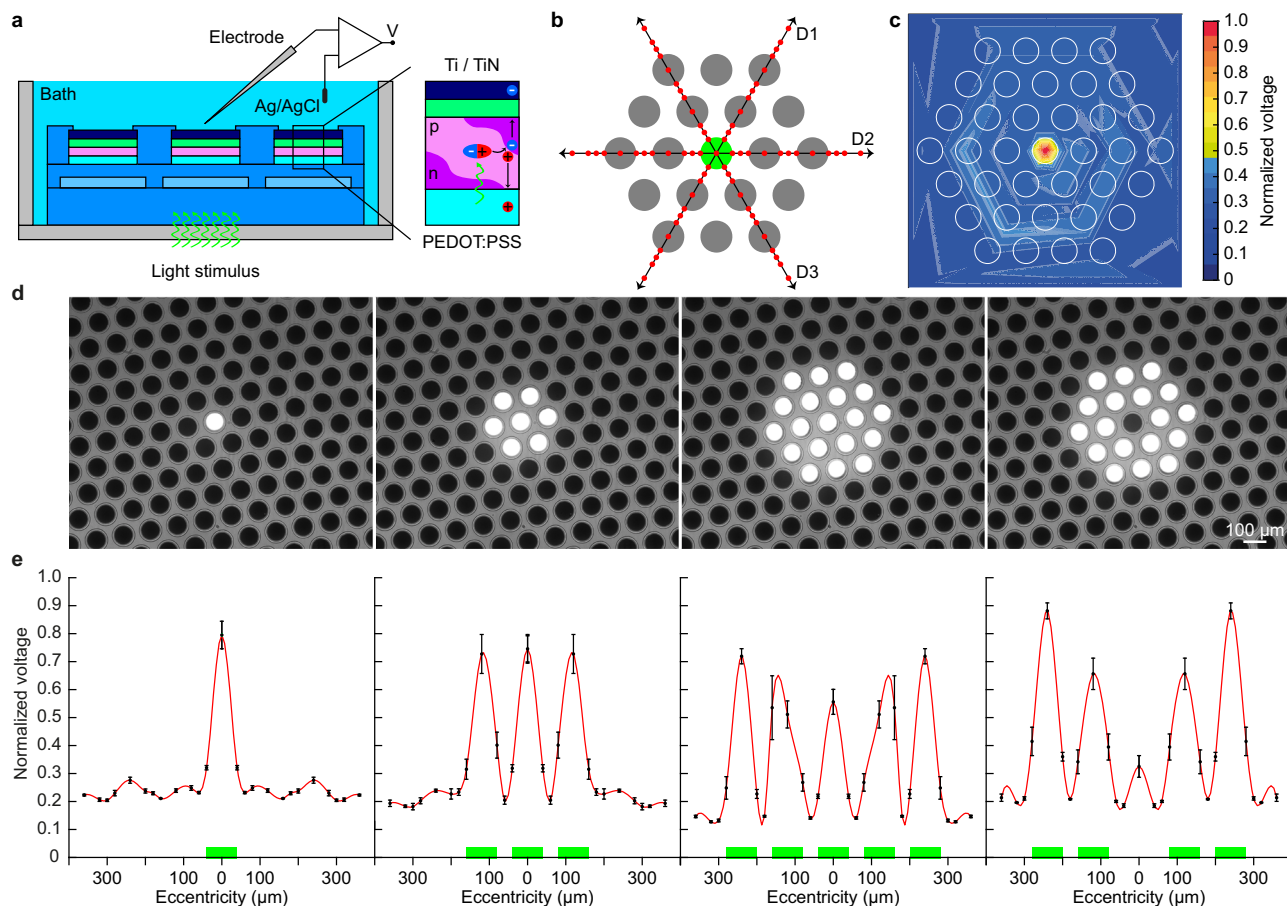
Fig. 2 Stimulation selectivity of the photovoltaic pixel. a Sketch of the experimental setup to measure the voltage spreading. The insert shows the photovoltaic transduction mechanism. A photon is absorbed by the P3HT (p-type semiconductor, electron donor) and an exciton is formed. The exciton travels until it reaches the interface between P3HT and PCBM (n-type semiconductor, electron acceptor) and dissociates. The electron is attracted towards the cathode (Ti/TiN), and the hole is attracted towards the anode (PEDOT:PSS) because of their work function levels. **b** Sketch of the experimental methodology. The green dot corresponds to the illuminated pixel (560 nm, 10 ms, 22 mW mm^{-2}). The grey ones represent the surrounding pixels. The voltage was measured in 25 positions (red dots) for each direction (D1, D2 and D3). **c** Voltage spreading colour map generated by interpolating the experimental measures with a triangulation-based linear interpolation. For each data point, ten consecutive recordings were averaged and the voltage peaks were normalised to the maximal value obtained in the whole experiment. The white circles show the location of the pixels. **d** Pictures of the four stimulation patterns: central on (left), central on and one corona on (middle left), central on and two coronas on (middle right), and central off and two coronas on (right). The light spots are visible (brighter area). **e** Normalised voltage profiles obtained for the four illumination patterns (mean ± s.e.m.; $n = 4$ prostheses). For each prosthesis, the normalised data from the three directions were averaged. The red line shows a Gaussian fitting, and the green bars beneath corresponds to the active pixels.

pixel. In fact, the TiN coating produces a more homogeneous film than Ti alone, with better contact and likely decreasing the series resistance. In turns, a lower series resistance reduced the current flowing into the shunt resistance of the device, especially at the light onset, hence increasing the PCD peak. It is worth to mention that the additional fabrication steps needed to process the TiN layer might also influence the polymer layer underneath and lead to higher PCD. These results open up the possibility of high-resolution single-pixel stimulation of RGCs.

Single-pixel stimulation efficiency of titanium nitride photovoltaic pixels. We subsequently evaluated whether the increased photovoltaic performances of TiN-coated pixels translated into a higher stimulation efficiency of RGCs. For the study, we used explanted retinas from the retinal degeneration 10 (rd10) mouse model, which is an established model for retinitis pigmentosa[40–42]. In agreement with our previous study[43] and studies performed by other laboratories[44,45], rd10 retinas beyond post-natal day (P) 60 can be considered light-insensitive. In order to ensure a proper

exclusion of intrinsic light responses due to spared photoreceptors, the experiments in this work were performed in rd10 retinas at a very late stage of degeneration (mean age ± s.d.: 127.2 ± 14.9). Both male and female mice were used to exclude any sex-related differences in the degeneration onset and progression (Table 3). Explanted retinas were layered in epiretinal configuration, and the prosthetic-evoked activity of RGCs was recorded via single-electrode extracellular recordings (Fig. 4a). Light pulses (560 nm, 10 ms) were delivered in a broad range of irradiance levels (0.9, 2.34, 6.24, 12.37, 17.68 and 22.65 mW mm^{-2}) and the network-mediated medium-latency (ML) responses of RGCs to large-field (covering ~70 pixels) illumination (Fig. 4b) and single-pixel illumination (Fig. 4c) were compared. Ten consecutive light pulses were delivered at 1 Hz for each illumination condition.

In the first set of cells ($n = 20$ RGCs for Ti pixels and $n = 21$ RGCs for TiN-coated pixels), the quantification of the ML spiking activity upon large-field illumination revealed that TiN-coated pixels elicited on average higher ML spiking activity than Ti pixels (Fig. 4d). Moreover, in both conditions, the first irradiance tested (0.9 mW mm^{-2}) elicited a statistically significant ML
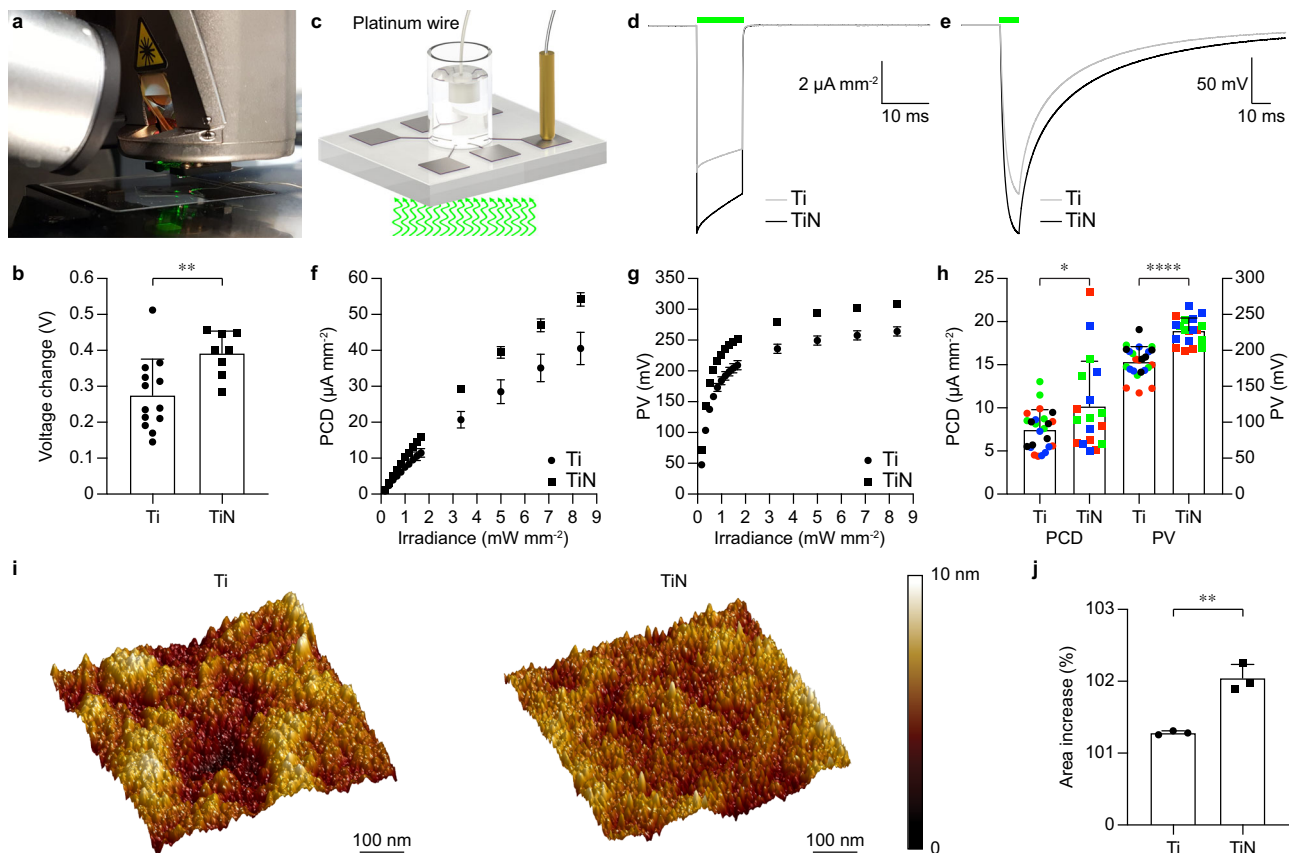
Fig. 3 Optoelectronic characterisation of the photovoltaic pixel. a Picture of the KPFM setup. **b** Surface voltage changes obtained with Ti (circles) and TiN-coated (squares) cathodes. Each bar is the mean (± s.d.) of the measures from $n = 13$ Ti pixels and $n = 8$ TiN-coated pixels. **c** Drawing of the experimental setup for the measure of the PC and PV; the light pulse comes from the bottom. **d**, **e** Mean PCD (**d**) and PV (**e**) measures obtained from Ti (grey) and TiN-coated (black) pixels upon illumination (565 nm, 10 ms, 0.9 mW mm^{-2}). For Ti, $n = 24$ pixels from four chips were averaged; for TiN, $n = 18$ pixels from three chips were averaged. **f**, **g** Mean (± s.e.m) PCD (**f**) and PV (**g**) amplitudes quantified at increasing irradiance levels (565 nm, 10 ms) for Ti pixels (circles; $n = 24$ pixels from four chips) and TiN-coated pixels (squares; $n = 18$ pixels from three chips). **h** Mean (± s.e.m) PCD and PV amplitudes quantified at 0.9 mW mm^{-2} for Ti ($n = 24$ pixels from four chips) and TiN-coated ($n = 18$ pixels from three chips) pixels. **i** AFM images of the Ti and Ti/TiN surfaces. The colour bar shows the surface roughness. **j** Mean (± s.d.) percental increase of the surface area compared to the nominal flat area (500 × 500 nm^2).

spiking activity higher than the basal activity computed without light (Ti: $P = 0.0088$; TiN: $P < 0.0001$; two-tailed unpaired t test). When the illumination was switched to single-pixel (Fig. 4e), both Ti and TiN-coated pixels also evoked a statistically significant ML spiking activity at the first irradiance tested (0.9 mW mm^{-2}; Ti: $P = 0.0378$; TiN: $P = 0.0062$; two-tailed unpaired t test). This result revealed that both Ti and TiN-coated photovoltaic pixels induced RGC activity upon single-pixel illumination.

Next, we quantified the fraction of RGCs that could be activated with 10-ms pulses at 0.9 mW mm^{-2} under both large-field and single-pixel stimulation. For Ti pixels and large-field stimulation, 16 out of 20 RGCs showed ML responses at 0.9 mW mm^{-2}, or in other words, exhibited an activation threshold lower or equal to 0.9 mW mm^{-2}. Three out of 20 RGCs showed activation at 2.34 mW mm^{-2}, and 1 out of 20 RGCs showed activation at 12.37 mW mm^{-2}. Switching to single-pixel illumination, only one-third of the RGCs (7 out of 20) preserved ML activity upon illumination at 0.9 mW mm^{-2}. For TiN-coated pixels, all RGCs (21 out of 21) showed ML activity upon large-field illumination at 0.9 mW mm^{-2}, and still more than half RGCs (12 out of 21) when the illumination was switched to single-pixel. This result shows the higher efficiency in single-pixel retinal stimulation of TiN-coated photovoltaic pixels compared to Ti pixels. Noteworthy, this increase in efficiency cannot be

attributed to sex-related differences. For Ti pixels, nine animals were used (129.4 ± 15.6, mean age ± s.d), of which seven males (77.8%) and two females (22.2%). For TiN-coated pixels, six animals were used (126.5 ± 22.0, mean age ± s.d), of which four males (66.7%) and two females (33.3%). Also, the mice's age was not statistically different among the two groups ($P = 0.77$, two-tailed unpaired t test). With TiN-coated pixels and single-pixel illumination, 57% (12 out of 21) of the recorded cells could be activated at 0.9 mW mm^{-2}, while the others required higher irradiance: a result coherent with those obtained by another photovoltaic retinal prosthesis[46]. The variation in the irradiance threshold can be related to the location of the RGC and its presynaptic network compared to the position of the illuminated pixel, which cannot be precisely located due to the recording method. Therefore, RGCs having their presynaptic network centred over a pixel might have a lower threshold than those RGCs eccentric to the pixel because of the very limited lateral spreading of the photovoltaic stimulus.

In the second set of cells ($n = 30$ RGCs) exhibiting ML response upon single-pixel illumination of TiN-coated pixels at 0.9 mW mm^{-2}, we determined the threshold for activation using lower irradiance levels (0.014, 0.16, 0.35, 0.68 and 0.9 mW mm^{-2}; ten consecutive light pulses were delivered at 1 Hz for each irradiance). The average ML firing rates upon single-pixel
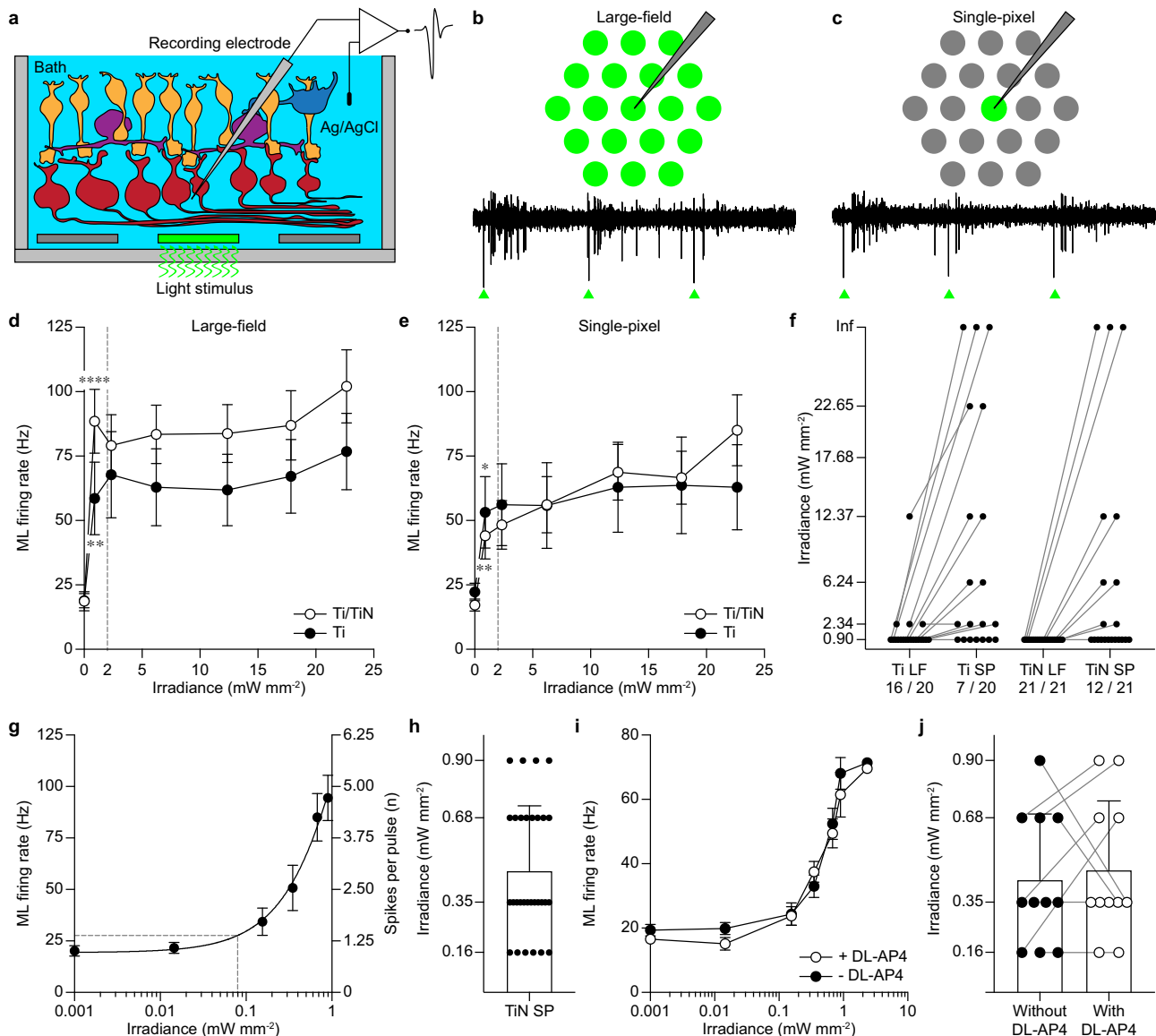
Fig. 4 Single-pixel stimulation of retinal ganglion cells. a Sketch of the recording setup. **b, c** Representative responses from a retinal ganglion cell upon three consecutive light pulses (560 nm, 10 ms, 0.9 mW mm^{-2}) with large-field illumination (**b**) and single-pixel illumination (**c**). The green triangles correspond to the onset of each pulse. **d, e** Comparison of the stimulation efficacy during large-field (**d**) and single-pixel (**e**) illumination under increasing irradiances with Ti-based ($n = 20$ RGCs, mean ± s.e.m.) and TiN-based pixels ($n = 21$ RGCs, mean ± s.e.m.). **f** Change in the activation threshold from large-field to single-pixel illumination for both Ti pixels ($n = 20$ RGCs) and TiN-coated pixels ($n = 21$ RGCs). The numbers for each column are the fraction of RGCs activated by a 10-ms light pulse of 0.9 mW mm^{-2}. Inf means that the RGC does not show ML activity at any of the irradiance levels tested. LF large-field, SP single-pixel. **g** ML firing rate ($n = 30$ RGCs, mean ± s.e.m.) at low irradiance levels for TiN-coated pixels and single-pixel illumination. The black line is the second-order polynomial interpolation ($R^2 = 0.29$). The grey dashed lines show the activation threshold computed as the irradiance eliciting 10% of the maximal ML firing rate at 0.9 mW mm^{-2}. The right axis shows the quantification of the average numbers of spikes elicited per light pulse. **h** Activation threshold for each RGCs with single-pixel illumination and TiN-coated pixels (mean ± s.d.). **i** ML firing rate ($n = 11$ RGCs, mean ± s.e.m.) at low irradiance levels for TiN-coated pixels and single-pixel illumination before and after the application of DL-AP4. **j** Activation threshold for each individual RGC with single-pixel illumination and TiN-coated pixels before (black circles) and after (white circles) the application of DL-AP4 (mean ± s.d.).

illumination increased as a function of the irradiance (Fig. 4g) with an activation threshold of ~79 μW mm^{-2}, obtained as the irradiance level providing 10% of the maximal ML firing rate measured at 0.9 mW mm^{-2}. This result shows that the responsivity of the RGCs can be modulated as a function of the irradiance level. However, we observed that the single-pixel activation threshold for individual RGCs was variable (Fig. 4h), and more than half (18 out of 30) of the RGCs exhibited an ML response threshold lower or equal to 0.35 mW mm^{-2}. While the population threshold was estimated to be 79 μW mm^{-2}, only 6 out of 30 cells

showed ML responses at 160 μW mm^{-2}. As before, the disparity of the network-mediated ML activation thresholds can be related to the location of the cell and its presynaptic network compared to the position of the illuminated pixel. Last, we evaluated in a subset of RGCs ($n = 11$ RGCs) the ML responsivity with and without the application of a broad spectrum glutamatergic synaptic antagonist (DL-AP4, 250 μM l^{-1}; No. 0101, Tocris Bioscience), which blocks the synaptic input of ON BCs[47] (Fig. 4i). The ML response curve was not altered by the introduction of the antagonist, thus excluding any contribution from potential spared photoreceptors

to the ML responses recorded upon photovoltaic stimulation. Also, the single-pixel activation threshold measured in individual RGCs was not statistically different after DL-AP4 application (Fig. 4j; $P = 0.68$, two-tailed paired t test).

These results confirmed that the network-mediated stimulation of RGCs in the epiretinal configuration is achieved with single-pixel illumination at irradiance levels largely below the maximum permissible exposure (MPE) limit for retinal safety, which for POLYRETINA varies between 8.32 and 2.08 mW mm^{-2}, respectively, for 5 and 20 Hz illumination rate and 10-ms pulse duration.

Photovoltaic receptive fields. Using TiN-coated pixels and single-pixel illumination at 0.9 mW mm^{-2}, we quantified in a third set of cells ($n = 31$ RGCs) the number of pixels electing a network-mediated ML response in a RGC (Fig. 5). The 19 neighbouring pixels around the recording electrode were successively illuminated (560 nm, 10 ms, 0.9 mW mm^{-2}, 1-Hz illumination rate) according to a counterclockwise pattern which was repeated ten times (Fig. 5a). The network-mediated ML activities elicited by the illumination of each pixel were mapped to the pixel coordinates, and the photovoltaic receptive fields (RFs) of the RGCs were fitted with a two-dimensional Gaussian model. Each RF diameter was then calculated as the average between the horizontal and vertical standard deviation of its two-dimensional activation map. The majority of the recorded RGCs (24 out of 31 cells) exhibited small RFs with a radius ranging from 34.5 to 142.5 μm (Fig. 5d). Five out of 31 RGCs exhibited large RFs whose radius varied between 184.3 and 282.7 μm (Fig. 5e). Two out of 31 RGCs exhibited elongated RFs, showing high responses to several aligned pixels (Fig. 5f). The activation maps of the RGCs could be clustered (Gaussian mixture model) into two populations (Fig. 5b), namely those exhibiting small or large RFs (RGCs with elongated RFs were excluded from the analysis). For clustering, the RFs were rotated so that the horizontal direction (x axis) corresponds to the axis of maximal dispersion and the vertical direction (y axis) corresponds to the dispersion in the orthogonal direction. The average photovoltaic RF diameter for each population was respectively 153.7 ± 26.1 μm and 335.5 ± 49.3 μm (mean ± s.e.m). Statistical analysis revealed that RGCs with small photovoltaic RFs could be stimulated through an average of three photovoltaic pixels (Fig. 5c). A pixel was considered to induce statistically significant activation of the RGC if the mean ML response, evaluated over ten repetitions, was statistically significantly higher than the cell background activity ($P < 0.05$, two-tailed unpaired t test), which was calculated as the activity in the 100-ms pre-stimulus period averaged across all the illuminated pixels. Cells with very small photovoltaic RFs could be activated by one pixel only. The larger the photovoltaic RF size, the higher the number of pixels stimulating the RGC. However, the number of pixels activating one RGC might also be affected by the actual centring of the cell and its presynaptic network compared to the photovoltaic pixels: a single RGC can be activated by multiple neighbouring pixels when it is centred in between the pixels.

The spatial resolution of the high-density POLYRETINA. The retina desensitises upon repetitive and static network-mediated stimulation, and the RGC spiking response decays proportionally to the stimulation frequency[48–50]. Taking advantage of this desensitisation process (adaptation to static stimulation), we investigated the stimulation response resolution using a two-point discrimination pattern reversal paradigm (pixel switch). In the fourth set of cells ($n = 12$ RGCs) upon repetitive stimulation from the same pixel at 5 Hz (560 nm, 10 ms, 0.9 mW mm^{-2}, 10 pulses), the response

desensitisation could be observed already at the second light pulse, and it reached a steady-state close to the average resting activity, calculated as the activity in the 100-ms pre-stimulus period averaged across all the RGCs (Fig. 6a–c). We stimulated RGCs with the two most responding pixels for each cell within their photovoltaic RFs (Fig. 6d). Upon repetitive stimulation from the first pixel at 5 Hz (560 nm, 10 ms, 0.9 mW mm^{-2}, five pulses), the desensitisation could also be observed from the second light pulse (Fig. 6e, f) with a $27.3 \pm 11.2\%$ drop in the ML firing rate (mean ± s.e.m.) compared to the first pulse response ($P = 0.0105$, two-tailed paired t test). However, the ML response was fully recovered at the pixel switch. To evaluate the response recovery, we computed a recovery threshold (red dashed line in Fig. 6f) defined as the central value between the naive ML response (i.e., to the first pulse in the sequence) and the average desensitised ML response (average over pulses 3, 4 and 5; cyan dashed line in Fig. 6f). The ML response at the pixel reversal exceeded the threshold and it was statistically significantly higher than the desensitised response ($P = 0.0226$, one-tailed paired t test). Moreover, the ML response at the pixel reversal was not statistically different from the naïve response to the first pulse ($P = 0.9054$, two-tailed paired t test).

A strong ML response to the first pulse from each pixel but not during the steady stimulation with the same pixel indicates that RGCs stimulated with POLYRETINA were able to resolve the spatial difference between the two pixels, allowing two-point discrimination of 120 μm (equivalent to the pixel pitch).

Next, in the fifth set of cells ($n = 26$ RGCs), we tested spatial resolution with a high-contrast grating pattern reversal paradigm, with a fixed bar width of 120 μm (Fig. 7a). Among the cells, we found three main behaviours presumably due to a variable alignment of the RGC presynaptic network with the illuminated bar: RGCs responding to the first pattern and the two reversals (Fig. 7b, top row), RGCs responding to the first pattern and the second reversal (Fig. 7b, middle row) and RGCs responding only to the first reversal (Fig. 7b, bottom row). Cumulatively, the ML response is reduced upon 5-Hz repetitive stimulation with a steady grating pattern (Fig. 7c), but it is recovered at the two reversals of the pattern (pulses 6 and 11). As before, we defined a recovery threshold for each reversal (red dashed lines in Fig. 7c) as the central values between the ML firing rate in response to the first pulse delivered with the previous pattern (pulse 1 and pulse 6 respectively for the first and the second reversal) and the average desensitised ML firing rate before the reversal (averaged over the ML responses to pulses 3, 4 and 5 for the first reversal and pulses 8, 9 and 10 for the second reversal; cyan dashed lines in Fig. 7b). The ML response to the first and second pattern reversals (pulse 6 and 11) exceeded their respective recovery thresholds (red dashed lines in Fig. 7c), and they were statistically significantly higher than the corresponding desensitised firing rate ($P = 0.0081$ and $P = 0.0140$, respectively, for the first and the second reversal, one-tailed paired t test). Moreover, the ML response to the grating reversals was not statistically different from the response to the first naïve pulse in the sequence ($P = 0.8971$ and $F = 0.0893$, repeated measure one-way ANOVA among responses to pulses 1, 6 and 11). These results demonstrated that RGCs stimulated with POLYRETINA could resolve 120-μm wide gratings.

The determine the spatial resolution limit, the grating pattern reversal paradigm was repeated with variable bar widths (200, 160, 120, 100 and 70 μm) in a subset of cells ($n = 18$ RGCs). The grating resolution of individual RGCs was assessed as the smallest grating size whose at least one reversal elicits a ML response at least two-third higher than the corresponding average desensitised ML firing rate (Fig. 8a). In other words, if the ML activity at pulse 6 is 1.66 higher than the average ML activity over pulses 3–5 or the ML activity at pulse 11 is 1.66 higher than the average ML activity over pulses 8–10. When varying the grating size, the
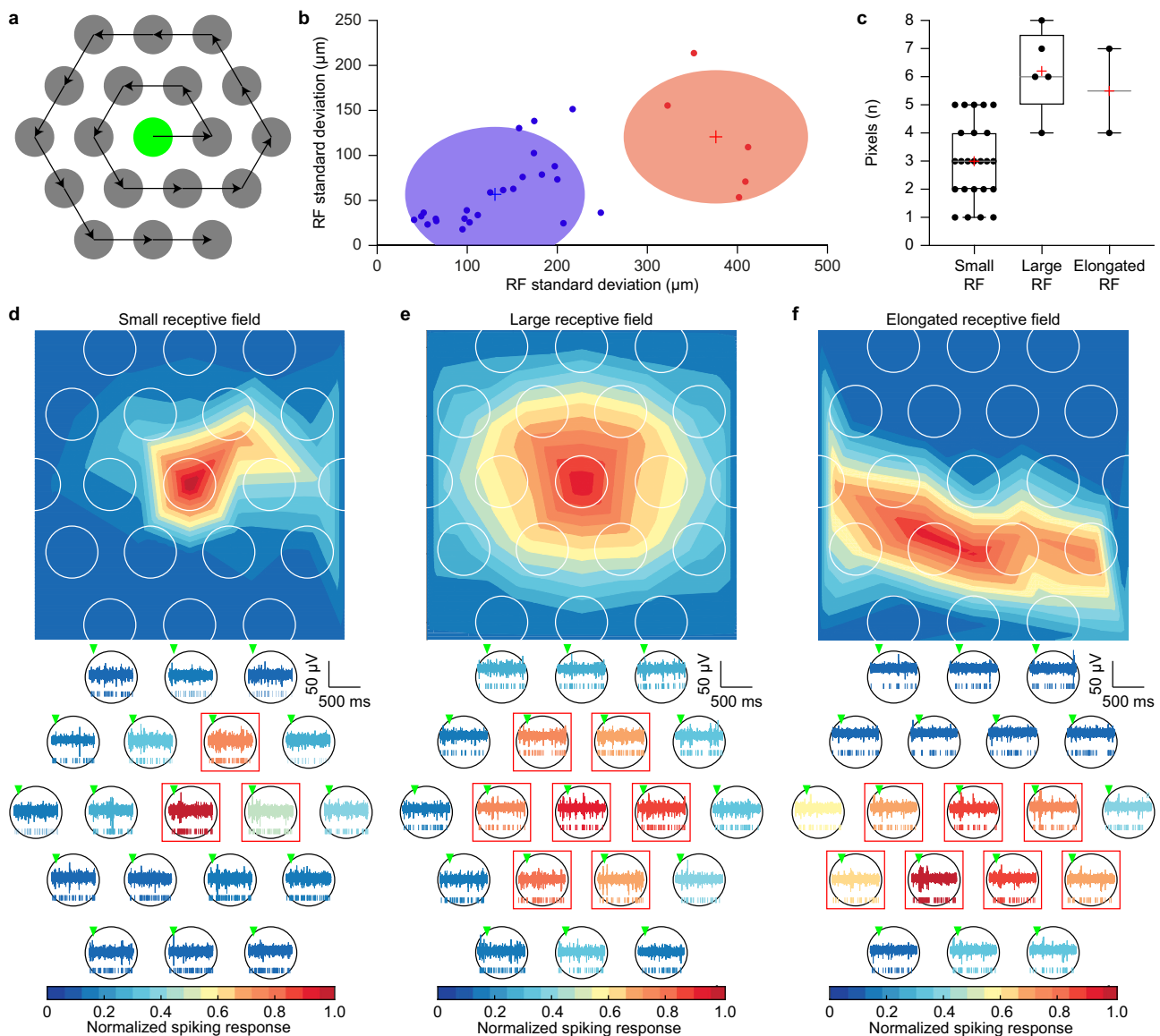
Fig. 5 Photovoltaic epiretinal receptive fields. a Sketch of the temporal pattern used for stimulation. Each of the 19 pixels centred around the recording location was successively illuminated following a counterclockwise pattern (560 nm, 10 ms, 0.9 mW mm^{-2}). The total illumination sequence was repeated for ten consecutive sweeps. The photovoltaic RFs were obtained by two-dimensional Gaussian approximation of the network-mediated ML responses elicited by single-pixel, averaged over sweeps, and normalised to the maximal responding pixel. **b** Gaussian mixture model of the photovoltaic RF sizes over the small ($n = 24$ RGCs, blue) and large RGC populations ($n = 5$ RGCs, red). The average photovoltaic RF diameter of the small and large cells types are, respectively, of 153.7 ± 26.1 µm and 335.5 ± 49.3 µm (mean ± s.e.m.). **c** Quantification of the number of pixels able to induce statistically significant ($P < 0.05$) ML activation in the recorded RGC. The horizontal grey line is the median, the red plus is the average and the boxes extend from the 25th to 75th percentiles. **d–f** Photovoltaic RFs from three individual RGCs classified as small RF cell (**d**), large RF cell (**e**) and elongated RF cell (**f**). The bottom panels show raw electrophysiological recordings and raster plots from the same cells for each single-pixel illumination (560 nm, 10 ms, 0.9 mW mm^{-2}, first sweep). The red boxes show the pixels inducing a statistically significant activation of the recorded RGC.

alignment of the cell's presynaptic network and the illuminated bar varied, and ML responses were observed either at the first pattern and the two reversals, at the first pattern and the second reversal or at the first reversal only (Fig. 8a). While the majority of the recorded cells RGCs (shows a response resolution matching the pixel pitch (120 µm, 7 out of 18) or slightly higher (100 µm, 6 out 18) or slightly higher (100 µm, 6 out 18), the remaining cells have either a response resolution lower than the pixel pitch (160 µm, 1 out of 18; 200 µm, 1 out of 18) or higher than the pixel pitch (70 µm, 3 out of 18) (Fig. 8b). Response resolutions higher than the pixel pitch could be explained by nonlinear integration in RF's subunits, as previously reported[51].

Last, in the sixth set of cells ($n = 12$ RGCs), we verified that the responses obtained at the pixel switch or the pattern reversal were not induced by a change in the stimulus contrast. Thus, we evaluated RGC's responses to irradiance steps without spatial content. RGCs were successively stimulated with large-field illumination (covering approximately 70 pixels) at three irradiance levels (0.9, 2.34 and 0.35 mW mm^{-2}) at 5-Hz illumination rate; five consecutive pulses were delivered for each irradiance level (Fig. 9a). No ML response recovery was observed for both the positive (from 0.9 to 2.34 mW mm^{-2}) and the negative (from 2.34 to 0.35 mW mm^{-2}) irradiance steps (Fig. 9b). The ML firing rates at the two irradiance steps (pulses 6 and 11) were not
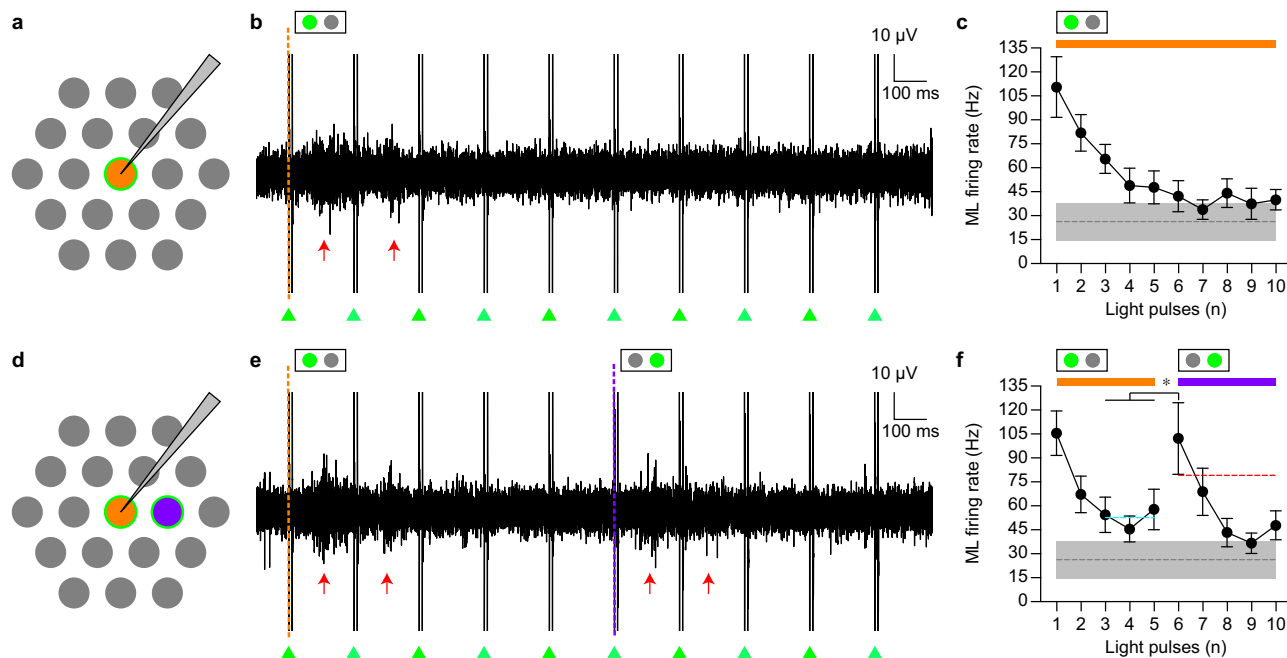
Fig. 6 Two-point discrimination pattern reversal test with single-pixel stimulation. a Sketch of the single-pixel repeated stimulation paradigm. One pixel was repeatedly illuminated at 5 Hz (560 nm, 10 ms, 0.9 mW mm^{-2}) for 2 s. **b** Raw electrophysiological recordings of a single RGC under 5 Hz continuous stimulation from a single pixel. The green triangles correspond to the onset of each pulse. The red arrows highlight the ML activity. **c** Quantification of the ML firing rate (mean ± s.e.m.) under continuous stimulation from a single pixel ($n = 12$ RGCs). The grey dashed line is the average resting firing rate with its s.d. represented by the grey area. **d** Sketch of the two-point discrimination pattern reversal paradigm. The central (orange) pixel was repeatedly illuminated for 1 s at 5 Hz (560 nm, 10 ms, 0.9 mW mm^{-2}), then the illumination was switched to the adjacent pixel (purple) for 1 s at 5 Hz (560 nm, 10 ms, 0.9 mW mm^{-2}). **e** Raw electrophysiological recordings of a single RGC under 5 Hz two-point discrimination pattern reversal paradigm. The green triangles correspond to the onset of each light pulse. The pixel switch is highlighted by the purple dashed line. The red arrows highlight ML activity. **f** Quantification of the ML firing rate (mean ± s.e.m.) under the two-point discrimination pattern reversal paradigm ($n = 12$ RGCs). The cyan dashed line is the average desensitised ML firing rate and the red dashed line is the recovery threshold. The grey dashed line is the average resting firing rate with its s.d. represented by the grey area.

statistically significantly higher or lower than the corresponding desensitised responses ($P = 0.1224$ and $P = 0.8546$, respectively, for the first and the second irradiance step, two-tailed paired t test). This result excludes responses due to changes in the stimulus irradiance. A small increase in the overall ML firing rate was observed by increasing the stimulus irradiance (pulses from six to ten). This increase was expected since the ML activity is irradiance dependent (Fig. 4).

In summary, this set of experiments confirmed a spatial resolution of the high-density POLYRETINA at least equivalent to its pixel pitch (120 Jim).

Design constraints for thermal safety. POLYRETINA achieved network-mediated stimulation of RGCs with single-pixel illumination at irradiance levels below the MPE limit for retinal safety. However, retinal damage is not the only element to be considered. During photovoltaic stimulation, a light beam is projected into the pupil, which might be transiently focused on the iris during involuntary large eye movements. In such a case, the temperature of the iris should not increase more than 2 °C (ISO 14708-1:2014/ EN 45502-1:1997). We performed a finite element analysis simulation, based on the worst-case scenario in which the full beam at the retinal MPE was stationarily projected onto the iris for a prolonged period. According to the calculated MPE for retinal safety, 47.90 mW at 565 nm could enter the pupil for chronic exposure for an illuminated retinal area of 127.97 mm^2 (43°). Given a constricted pupil of ~3 mm (as considered in the safety standard[52]) and a light beam reduced to a spot of 2 mm in diameter (to avoid beam clipping), the resulting irradiance at the

iris plane is 15.25 mW mm^{-2}. Due to the axial symmetry of the thermal simulation, we modelled the iris as a continuous tissue without a pupil (Fig. 10a). The temperature in the iris increased by 13.58 °C after 150 s of continuous illumination at the MPE (Fig. 10b, red line), which is largely above the safety limit of 2 °C. In order to keep the chronic thermal increase in the iris below 2 °C, the irradiance should be reduced to 2.25 mW mm^{-2} (Fig. 10b, green line), corresponding to a total of 7.07 mW chronically entering from the pupil. At the retinal level, this irradiance would correspond to a maximum of 1.1 mW mm^{-2} for 10-ms pulses, 5 Hz repetition rate, and an illuminated area of 127.97 mm^2, which is above the irradiance threshold for single-pixel stimulation of RGCs.

However, it is unlikely that the beam remains statically focused on the same area of the iris for 150 s, as the continuous eye movements would spread the light beam over a larger area and reduce its thermal impact[52]. Therefore, we quantified the time needed to reach 2 °C with a stable beam (Fig. 10c, black line and circles). At 15.25 mW mm^{-2}, an increase of 2 °C is reached after 460 ms, and the time increases by decreasing the irradiance at the iris plane: at 3.25 mW mm^{-2}, an increase of 2 °C is reached after 8.5 s. It is reasonable to consider that eye movements will reduce the thermal impact (as stated in the safety standard[52]). Therefore, the maximal irradiance entering the pupil can be further increased well above the irradiance threshold for single-pixel stimulation of RGCs compared to the worst-case scenario. Moreover, eye-tracking sensors embedded in modern virtual reality glasses provide tracking at 120 Hz, thus allowing real-time adjustment of the beam based on the eye gaze. Under a working hypothesis of 10-ms pulses repeated at 5–20 Hz, the eye tracker
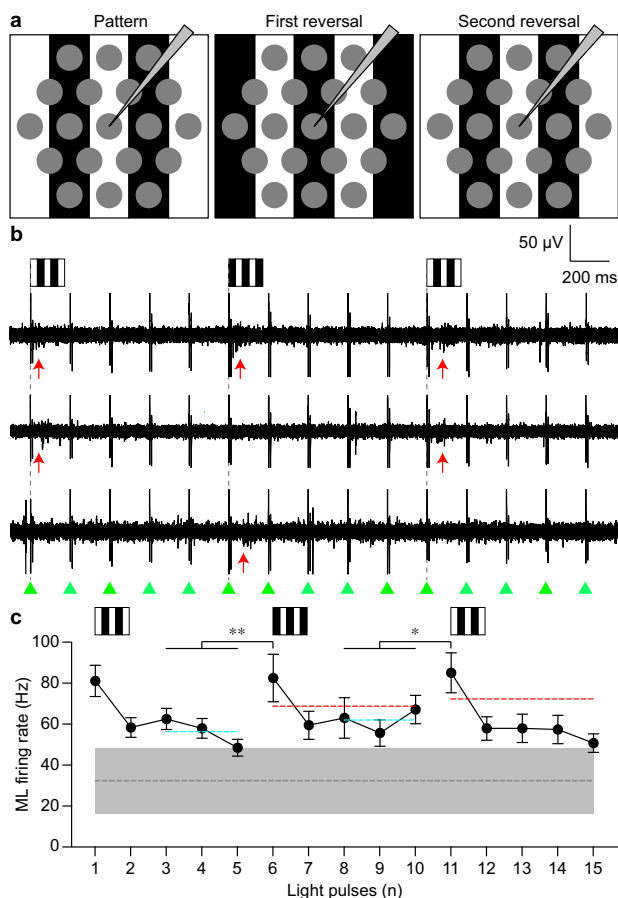
Fig. 7 Grating pattern reversal with a fixed bar width. a Sketch of the grating pattern reversal with a fixed bar width. A grating pattern with black and green 120-μm wide vertical bars (560 nm, 10 ms, 0.9 mW mm^{-2}) was projected onto the array with a 5-Hz illumination rate for 3 s and reverted every five pulses. **b** Raw electrophysiological recordings of three RGCs under grating pattern reversal with a fixed bar width. The green triangles correspond to the onset of each light pulse. The first pattern and the reversals are highlighted by the grey dashed lines. The red arrows highlight ML activity. **c** Quantification of the ML firing rate (mean ± s.e.m.) under grating pattern reversal with 120-μm bar width ($n = 26$ RGCs). The cyan dashed lines are the average desensitised ML firing rates and the red dashed lines are the recovery thresholds. The grey dashed line is the average resting firing rate with its s.d. represented by the grey area.

will have enough time to correct the projection system by using a steering mirror or, in the worst case, to close the beam to preserve the iris. Therefore, the obtained retinal irradiance can be further increased (Fig. 10c, coloured lines), thus allowing high pulse rates.

Discussion

So far, the maximum number of electrodes embedded in retinal prostheses and their overall density was limited by implantable pulse generators, transscleral connections and feedlines in the array[33]. The photovoltaic technique in retinal prostheses allowed increasing both the electrode number and density in a single step. However, despite this advancement, the small size, high stiffness and low conformability of many devices limit the overall retinal coverage to few millimetres, and so the restored visual angle to ~6°[10,51]. The retinal coverage could be slightly increased by tiling small rigid implants, as shown in rabbits, but only up to a 3.5-mm diameter area (~11°)[53].

Conjugated polymers combined with stretchable substrates, such as in the POLYRETINA prosthesis, allows for photovoltaic
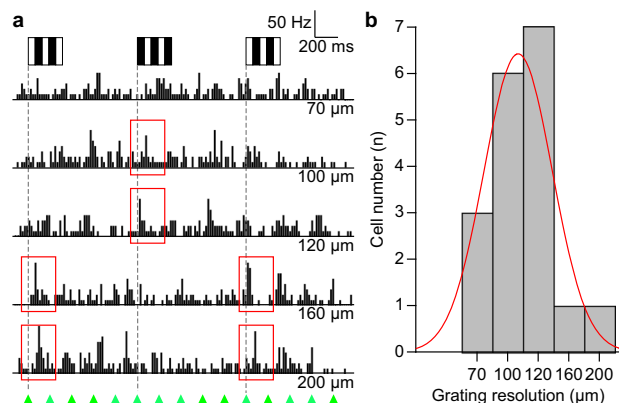

Fig. 8 Spatial resolution limit. a Peri-stimulus time histograms (bins of 10 ms) for one RGC upon grating pattern reversal stimulation with decreasing bar widths (200, 160, 120, 100 and 70 μm). A grating pattern with black and green vertical bars (560 nm, 10 ms, 0.9 mW mm^{-2}) was projected onto the array with a 5-Hz illumination rate for 3 s and reverted every five pulses. The first pattern and the reversals are highlighted by the grey dashed lines. The green triangles correspond to the onset of each light pulse. The red rectangles highlight ML activity. **b** Distribution of grating resolutions obtained in 18 RGCs.
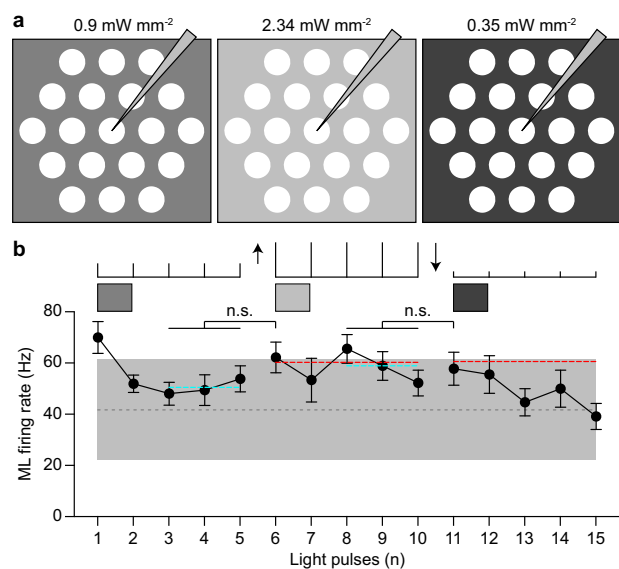

Fig. 9 Modulation of stimulus contrast without spatial content. a Sketch of the stimulus contrast modulation paradigm. Pixels were repeatedly illuminated with large-field illumination at 5 Hz (560 nm, 10 ms) for 3 s, and the irradiance level was changed every five pulses (0.9, 2.34 and 0.35 mW mm^{-2}). The first change was a step increase while the second change was a step decrease. **b** Quantification of the ML firing rate (mean ± s.e.m.) under modulation of the stimulus contrast without spatial content ($n = 12$ RGCs). The cyan dashed lines are the average desensitised ML firing rates and the red dashed lines are the recovery thresholds. The grey dashed line is the average resting firing rate with its s.d. represented by the grey area.

retinal stimulation together with a wide coverage of the retinal surface. Conjugated polymers were first introduced in retinal stimulation as continuous films directly interfaced with the retina[54–58] and already proved to be effective in vivo to restore visual acuity in blind rats[10]. In principle, a continuous film might be advantageous compared to discrete electrodes since the electrodes' fixed arrangement might limit the stimulation's spatial resolution. Focused stimulation with continuous films is possible
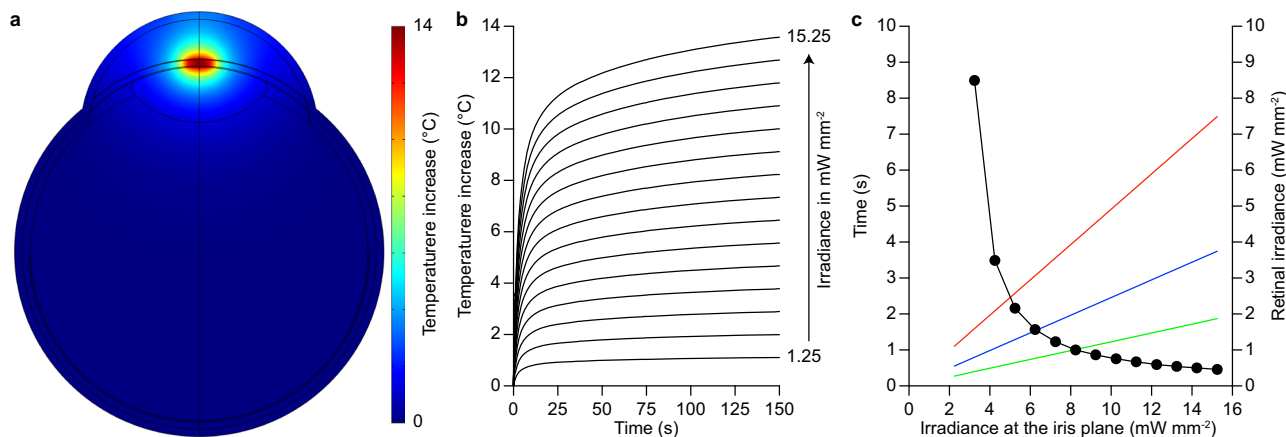
Fig. 10 Thermal simulations at the iris plane. a Temperature increase in the modelled eye after 150 s of continuous illumination on the iris at the MPE (565 nm, 15.25 mW mm^{-2}). **b** Quantification of the temperature increases at the iris plane during 150 s of continuous illumination for increasing irradiance levels from 1.25 to 15.25 mW mm^{-2} (increments of 1 mW mm^{-2}). **c** Quantification of the time to reach a thermal increase of 2 °C (left axis) as a function of the irradiance at the iris plane for continuous illumination at 565 nm (black circles and line). The coloured lines show the irradiance obtained at the retinal level (right axis) for ten pulses repeated at 5 Hz (red line), 10 Hz (blue line) and 20 Hz (green line) as a function of the irradiance at the iris plane for continuous illumination.

only with materials having low carrier mobility and lifetime, such as conjugated polymers[11]. A similar approach is now proposed with other materials, like TiO$_2$ nanotubes[59] and Au–TiO$_2$ nanowires[12]. However, while continuous films are interesting for small implants, they become more challenging for wide-field implants aiming at restoring a large visual angle. Inorganic materials might not be easily fabricated on conformable materials since they often require high-temperature processes. Polymers can be deposited on a large area, but they would immediately crack and eventually delaminate once stretched over a spherical surface. Therefore, pixels must be fabricated and protected to preserve their mechanical integrity like in the POLYRETINA device. The microscale patterning of conjugated polymers is an essential element to fabricate a high-density wide-field organic photovoltaic prosthesis: the high-density POLYRETINA has 10,498 physically and electrically independent pixels with a 120-μm pitch. The device's mechanical integrity was preserved thanks to the SU-8 platforms, the patterning of the conjugated polymers and the TiN coating, which reduces the tensile stress on the pixels. The device's mechanical compliance allows the bonding of the high-density array over a large and soft hemispherical dome to maintain close contact between the pixels and the retinal tissue over the central and peripheral retina. The TiN coating enhances the stimulation efficiency, improves mechanical stability and eases the fabrication process. Pixels were independently activated with a focused light pattern; the photovoltage generated largely remains localised within the pixel lateral boundaries, even at high irradiance levels, thus ensuring the absence of electrical crosstalk between the pixels.

Single-pixel illumination reproducibly evoked network-mediated ML activity in blind retinas at irradiance levels below the MPE limit. Indeed, POLYRETINA delivers a capacitive-like photovoltage optimal for network-mediated activation of the RGCs from the epiretinal side[43], provided that long (e.g., 10-ms) light pulses are used. The increase in the pixel's number and density resulted in epiretinal stimulation with high spatial resolution. In this study, we demonstrated a response resolution of the POLYTEINA device equivalent to at least its pixel's pitch (120 μm), using both a two-point discrimination test and a grating pattern reversal paradigm. Such resolution would theoretical corresponds to a visual acuity of 20/480[60], which place POLYRETINA in the upper intermediate level close to the

PRIMA and Alpha-AMS devices: a borderline resolution range for faces and emotions recognition[61]. Nevertheless, such a form of artificial vision may be valuable for a more reliable obstacle recognition and ambulation[15,62]. The primary difference between POLYRETINA and the aforementioned implants is its large visual angle, which impacts the perceived visual field. The combination of visual acuity and visual angle is recognised as a crucial need to map and interact with one's environment, having consequences on the layout space understanding, walking distance evaluation, identify-and-reach tasks, spatial cognition and attention[63,64]. Our study was conducted with degenerated mouse retinas. Compared to the human one, the mouse retina's peculiarity is to have RGCs with large and relatively homogeneous RFs, despite their eccentricities. The RGC's topography is organised in a dorsoventral axis, without any region devoted to high visual acuity[65,66]. Most RGCs in the mouse retina have natural RFs equal to or larger than the photovoltaic pixels' pitch within POLYRETINA[67]. In the perspective of clinical applications, it should be noted that the RGCs' dendritic fields in the human fovea are substantially smaller: 5–12 μm for midget cells and 30–40 μm for parasol cells[68,69]. The pixel's pitch would thus determine the theoretical resolution limit in the fovea and parafovea. However, in humans, the size of RFs and the arborisation of both midget and parasol cells increases with eccentricity[68–70]. POLYRETINA covers 43°, ~11–13% of the retinal surface[71,72], i.e., the fovea, the parafovea, the perifovea, and up to 6–7 mm away from the fovea in the mid-peripheral retina. The dendritic tree varies between 150 and 270 μm for parasol cells and between 25 and 70 μm for midget cells in the perifovea. In the mid-peripheral retina, it varies between 175 and 310 μm for parasol cells and between 50 and 120 μm for midget cells[68]. Outside of the fovea, both cell types have RF diameters equal to or larger than the pixel pitch in POLYRETINA. Based on our results in mice retinas, ~40% of the human RGCs, mostly parafoveal and mid-peripheral parasol cells but also mid-peripheral midget cells could be stimulated with a resolution higher than their physiological RFs.

The legal definition of blindness in the United States of America and most European countries does not only take into account the foveal acuity (worse than 20/200) but also the visual angle (smaller than 20°), because of its critical role in the naturalistic perception of complex scenes, movements and objects. Indeed, self-orienting task and free mobility in a moving

environment require the rapid detection of movements and luminance changes from the entire visual field. The restoration of a large visual field with appropriate resolution represents a leap forward for artificial vision. However, some steps are still required before considering POLYRETINA for a clinical trial. One open question is the distortion of phosphenes experienced by patients during epiretinal stimulation because of the direct activation of the axons of passage, which might have a negative impact on the perceived resolution. Previous results in patients implanted with the Argus® II device showed that phosphene's distortion could be reduced if not avoided by lengthening the duration of the stimulation pulse[13]. Results in explanted retinas[43,73,74] and computational models[43] suggested that the implementation of both long pulses and non-rectangular waveform (as the case for POLYRETINA) allows a preferential activation of RGCs via the network-mediated mechanism. Despite the direct activation of RGCs cannot be totally avoided, the probability to elicit short-latency direct spikes upon POLYRETINA stimulation was previously evaluated to be ~20% per light pulse[11], which corresponds to 0.2 spikes per light pulse: a very low spike rate, ~25 times lower than network-mediated ML spikes (about five spikes per pulse). It still remains unclear if those low probability short-latency direct spikes would be meaningful for the patients from a perceptual standpoint. Only human trials will answer this question.

Another limit of photovoltaic retinal prostheses based on conjugated polymers is the use of semiconducting materials absorbing light in the visible spectrum (e.g., P3HT). Visible light for prosthetic activation is not optimal due to the possible activation of remaining photoreceptors in patients with some residual vision. Moreover, the high irradiance levels required to activate POLYRETINA might be perceived even in blind patients without residual vision. Novel conjugated polymers with shifted sensitivity in the far-red and near-infrared could be exploited to overcome this problem[75,76]. Recent results reported the possibility to use a red-shifted polymer in neural interfaces[58] and retinal prostheses[75].

A third limit is set by the constraints imposed by the maximal irradiance, such as the maximal illumination rate. So far, retinitis pigmentosa patients implanted with retinal prostheses used low stimulation rates (e.g., 5–10 Hz)[5,77,78], which are within the safety limits for POLYRETINA. However, higher stimulation rates might be desirable to avoid flickering and achieve flicker fusion. It is unclear at this stage, which is the optimal stimulation frequency for a device like POLYRETINA and psychophysical studies will be required to characterise it. In order to achieve higher illumination rates, the thermal impact should be minimised: both near-infrared sensitive polymers and beam compensation strategies might be helpful. A reduction in the visual angle could also contribute to reduce the thermal impact. Although a wide-visual angle (i.e., above 30°) is highly desirable in profoundly and totally blind patients, only psychophysical tests can determine the exact minimum angle required. POLYRETINA covers 43°, but a reduction to 35° would increase the maximal irradiance at the iris plane by 50%. Last, the POLYRETINA's safety and efficacy should be validated in preclinical trials in vivo.

Methods
Mechanical simulations. Finite element analysis simulations were performed in Abaqus/CAE 6.14, using a three-dimensional deformable shell (photovoltaic interface) moving against a static spherical solid (hemispherical dome) to create a full hard contact. The edges of the shell were clamped to move only in the vertical direction towards the solid dome. The surface roughness and intrinsic thin-film stresses arising from deposition techniques were not considered in the simulation. The shell was constructed using the parameters listed in Table 1.

Thermal model. COMSOL Multiphysics 5.3 was used with the Bioheat module and the General PDE module for the heat transfer and Beer-Lambert light

Table 1 Mechanical simulations.

Material	Young's modulus (MPa)	Poisson's ratio	Density (kg m^{-3})
PDMS (Neo-Hookean)	$C_{10} = 0.662$, $D_1 = 0.255$	0.5	970
SU-8	2920	0.22	–
PEDOT:PSS	1900	0.34	–
P3HT: PC60BM	1970	0.35	–
Ti	90,000	0.34	–
TiN	220,000	0.25	–

PDMS polydimethylsiloxane, PEDOT poly(3,4-ethylenedioxythiophene), PSS poly (styrenesulfonate), P3HT regioregular poly(3-hexylthiophene-2,5-diyl), PC60BM [6,6]-phenyl-C61-butyric acid methyl ester, Ti titanium, TiN titanium nitride.
List of parameters used for the construction of the deformable shell. Apart from PDMS, the behaviours of the other materials were considered isotropic elastic. The values for Young's modulus and Poisson's ratio of the used materials and the hyperelastic coefficients for PDMS were taken from the following references[80-86].

propagation. A uniform beam with a diameter of 2 mm (565 nm) was used as the illumination source. The eye model was built with several spheres representing each component (cornea, aqueous humour, lens, iris anterior border layer, iris stroma, iris pigmented epithelium, vitreous humour, retina, retinal pigmented epithelium, choroid and sclera). The iris was simulated as a continuous film completely covering the pupil, while the light beam was projected on the iris, centred to the pupil location. All the parameters used in the model are listed in Table 2.

Chips microfabrication. Samples were fabricated on 20 × 24 mm² glass substrates (2947-75×50, Corning Incorporated) cleaned by ultrasonication in acetone, isopropyl alcohol, and deionised water for 15 min each and then dried with a nitrogen gun. PEDOT:PSS (PH1000, Clevios Heraeus) was mixed to 0.1 v/v% (3-glycidyloxypropyl)trimethoxysilane (440167, Sigma-Aldrich), filtered (1-μm PTFE filters), and then spin-coated at 3000 rpm for 40 s on each chip. Subsequent annealing at 115 °C for 30 min was performed. The preparation of the bulk heterojunction was performed in a glove box under nitrogen atmosphere. In total, 20 mg of P3HT (M1011, Ossila) and 20 mg of PC60BM (M111, Ossila) were dissolved in 1 mL of anhydrous chlorobenzene each and let stirring overnight (16 hr) at 70 °C. The solutions were then filtered (0.45-μm PTFE filters) and blended (1:1 v:v). The P3HT:PC60BM blend was spin-coated at 1000 rpm for 45 s. Subsequent annealing at 115 °C for 30 min was performed. Titanium and titanium nitride cathodes were deposited by direct-current (Ti) and radio frequency (TiN) magnetron sputtering using a shadow mask. The polymer patterning step was obtained by exposing the chips to oxygen plasma. A plastic reservoir was then attached to the sample using PDMS as an adhesive.

The measure of photovoltage and photocurrent. Samples were placed on a holder, and each electrode was sequentially contacted. A platinum wire immersed in physiological saline solution (NaCl 0.9%) was used as a counter electrode. In all, 10-ms light pulses were delivered by a 565-nm LED (M565L3, Thorlabs) focused at the sample level. Photovoltage and photocurrent were measured using respectively a voltage amplifier (1201, band DC-3000 Hz, DL-Instruments) and a current amplifier (1212, DL-Instruments). Data sampling (40 kHz) and instrument synchronisation were obtained via a DAQ board (PCIe-6321, National Instruments) and custom-made software. Data analysis was performed in MATLAB (MathWorks). When evaluating the photocurrent density generated by the interface, the area of the connecting line exposed to light was also considered.

POLYRETINA microfabrication. Photovoltaic interfaces were fabricated on silicon wafers. A thin sacrificial layer of poly(4-styrenesulfonic acid) solution (561223, Sigma-Aldrich) was spin-coated on the wafers (1500 rpm, 40 s) and baked (120 °C, 15 min). Degassed PDMS pre-polymer (10:1 ratio base-to-curing agent, Sylgard 184, Dow-Corning) was then spin-coated (1000 rpm, 60 s) and cured in the oven (80 °C, 2 h). After surface treatment with oxygen plasma (30 W, 30 s), a 6-μm thick SU-8 (GM1060, Gersteltec) layer was spin-coated (3800 rpm, 45 s), soft-baked (130 °C, 300 s), exposed (140 mJ cm⁻², 365 nm), post-baked (90 °C, 1800 s; 60 °C, 2700 s), developed in propylene glycol monomethyl ether acetate (48443, Sigma-Aldrich) for 2 min, rinsed in isopropyl alcohol and dried with nitrogen. After surface treatment with oxygen plasma (30 W, 30 s), the second layer of degassed PDMS pre-polymer (10:1) was spin-coated (3700 rpm, 60 s) and cured in the oven (80 °C, 2 h). PEDOT:PSS and P3HT:PC60BM were prepared and deposited as described before. Titanium and titanium nitride cathodes were deposited by direct-current (Ti) and radio frequency (TiN) magnetron sputtering using a shadow mask

Table 2 Eye parameters used for the eye model.

Material	Thickness	Heat capacity	Thermal conductivity	Density	Absorption (565 nm)	Perfusion rate	Self-heat
	μm	J kg^{-1}K^{-1}	W m^{-1}K^{-1}	Kg m^{-3}	m^{-1}	s^{-1}	W m^{-3}
Aqueous humour	3100	3997	0.58	1000	0.025	0	0
Choroid	430	3840	0.53	1050	15,000	0.0091	10,000
Cornea	500	4178	0.58	1050	51	0	0
Lens	3600	3000	0.4	1050	2.5	0	0
Retina	100	3680	0.565	1000	400	0	0
Retinal pigment epithelium	10	4178	0.603	1050	110,000	0	0
Sclera	500	4178	0.58	1000	590	0	0
Vitreous humour	/	3997	0.6	1000	0.025	0	0
Iris anterior border layer	50	4178	0.58	1050	5470	0	0
Iris stroma	400	3840	0.53	1050	2750	0.0091	10,000
Iris pigment epithelium	70	4178	0.603	1050	100,000	0	0

The heat capacity, thermal conductivity, density, perfusion rate and self-heat of the iris anterior border layer, stroma and pigment epithelium were taken respectively from the cornea, choroid and retinal pigment epithelium, due to their biological similarity.
The parameters were obtained from references[87–93].

aligned with the SU-8 pattern. After the patterning of polymers by oxygen plasma, the encapsulation layer of degassed PDMS pre-polymer (5:1 ratio) was spin-coated (4000 rpm, 60 s) and cured in the oven (80 °C, 2 h). Photolithography and PDMS dry etching were performed to expose the cathodes. The wafers were then placed in deionised water to allow for the dissolution of the sacrificial layer and the release of the photovoltaic interfaces. The floating membranes were finally collected and dried in air. The hemispherical PDMS domes were fabricated using a milled PMMA mould, filled with PDMS pre-polymer (10:1), which was then degassed and cured in the oven (80 °C, 2 h). The supports were released from the moulding parts and perforated with a hole puncher (330 μm in diameter) at the locations dedicated to the insertion of retinal tacks. The released photovoltaic interfaces were clamped between two O-rings and, together with the hemispherical domes, were exposed to oxygen plasma (30 W, 30 s). The activated PDMS surfaces were put in contact and allowed to uniformly bond thanks to radial stretching of the fixed membrane. The excessive PDMS used to clamp the array was removed by laser cutting.

Atomic force microscopy. AFM images and roughness measurements were obtained with a Bruker Dimension icon microscope and scanasyst-air Si tips. Images (500 × 500 nm^2) were plotted and the surface area was calculated with NanoScope analysis 1.9 software.

Kelvin probe force microscopy. KPFM characterisation was performed in ambient air conditions with a dimension icon atomic force microscope (Bruker Corporation) using n-doped silicon tips (SCM-PIT-V2, Bruker Corporation) in surface potential, amplitude-modulated imaging mode. KPFM images were collected by repetitively scanning a single 100-nm line under dark and light conditions to measure the surface potential variation. The green LED of a Spectra X illumination system (Emission filter 560/32, Lumencor) was used to illuminate the pixel using optical fibre and focused onto the pixel (Photo-Conductive accessory, Bruker Corporation). The samples were grounded using a silver paste; however, individual pixels could not be connected to the paste and were therefore floating. The voltage bias was sent to the AFM tip. KPFM images were analysed using Gwyddion 2.36 software. For each image, the average surface potential variation value was obtained by subtracting the surface potential in the dark to the one under illumination (voltage in light − voltage in the dark).

Spatial selectivity measures. Measures of the voltage spread were performed in Ames' medium (A1420, Sigma-Aldrich) at 32 °C with a glass micropipette (tip diameter ~10 μm) located ~2–5 μm from the implant surface. Data were amplified (Model 3000, A-M System), filtered (DC—1000 Hz), and digitalised at 30 kHz (Micro1401-3, CED Ltd.). Illumination was carried out on a Nikon Ti-E inverted microscope (Nikon Instruments) using a Spectra X illumination system (Emission filter 560/32, Lumencor). The microscope was equipped with a dichroic filter (FF875-Di01-25×36, Semrock) and a ×10 (CFI Plan Apochromat Lambda) objective. The patterning of the light stimulus was carried out using a light patterning system (Polygon 400, Mightex). The light pattern sequences were adjusted in real-time to align the light patterns to the prosthesis pixels (PolyScan, Mightex). After alignment of the illumination pattern onto the POLYRETINA pixels, ten pulses of 10 ms were delivered at 1 Hz with an irradiance of 22.65 mW mm^{-2}. Data analysis was conducted in MATLAB. Voltage peaks above noise level were detected, and their amplitude normalised with respect to the central pixel value.

Electrophysiology. Animal experiments were conducted according to the animal authorisations GE/37/17 and GE/31/20 issued by the Département de l'Emploi, des Affaires Sociales et de la Santé (DEAS), Direction Générale de la Santé of the République et Canton de Genève (Switzerland). Both male and female rd10 mice were used (Table 3). Mice were kept in a 12 h day/night cycle with access to food and water ad libitum. White light (300 ± 50 lux) was present from 7 AM to 7 PM and red light (650–720 nm, 80–100 lux) from 7 PM to 7 AM. Retinas from the inbred Rd10 mice colony were explanted in normal light conditions after the animals were sacrificed by injection of sodium pentobarbital (150 mg kg^{-1}). After eye enucleation, retinas were dissected in carboxygenated (95% O$_2$ and 5% CO$_2$) Ames' medium (A1420, Sigma-Aldrich) and transferred to the microscope stage for stimulation and recording. Retinas were placed with the retinal ganglion cells facing down on the prosthesis. Recordings were performed in dim light at 32 °C with a sharp metal electrode (PTM23BO5KT, World Precision Instruments), amplified (Model 3000, A-M System), filtered (300–3000 Hz), and digitalised at 30 kHz (Micro1401-3, CED Ltd.). Illumination was carried out on a Nikon Ti-E inverted microscope (Nikon Instruments) using a Spectra X illumination system (Emission filter 560/32, Lumencor). The microscope was equipped with a dichroic filter (FF875-Di01-25×36, Semrock) and a ×10 (CFI Plan Apochromat Lambda) objective. The patterning of the light stimulus was carried out using a light patterning system (Polygon 400, Mightex). The light pattern sequences were real-time adjusted to align the light patterns to the prosthesis pixels (PolyScan, Mightex). Spike detection and sorting were performed by threshold detection using the Matlab-based algorithm Wave_clus[79] and further data processed in MATLAB. An exclusion period of ±1 ms around light onset and offset was applied to avoid artefact misclassification. The time window for the quantification of the network-mediated medium-latency response was selected according to previous results with the POLYRETINA device, which evokes a 30–50-ms-long network-mediated medium-latency response[11,43,50]. For each stimulation pulse, the network-mediated medium-latency response was calculated as the average firing rate elicited in a 50-ms window around the highest bin of the peri-stimulus time histogram (five bins of 10 ms each). The highest bin was screened from 40 to 120 ms after the stimulus onset.

Optical safety. Retinal damage upon light exposure can occur because of three main factors: photo-thermal damage, photochemical damage and thermo-acoustic damage[52]. In ophthalmic devices, Maxwellian illumination is used where the incident illumination occupies a fraction of the pupil (no overfilling). For continuous illumination, the MPE could be controlled by the photo-thermal (MPE$_T$) or photochemical damage (MPE$_C$), calculated in W according to Eqs. (1) and (2), respectively.

$$\text{MPE}_T = 6.93 \cdot 10^{-5} C_E C_T \frac{1}{P} \tag{1}$$

$$\text{MPE}_C = 5.56 \cdot 10^{-10} C_B \alpha^2 \tag{2}$$

For POLYRETINA, the visual angle α is calculated according to Eq. (3), and the exposed area according to Eq. (4), in which $d = 13.4$ mm is the diameter covered by the active area and $f = 17$ mm is the eye's focal length.

$$\alpha = 2 \tan^{-1} \frac{d}{2f} = 750.85 \text{ mrad} \tag{3}$$

$$A \approx \frac{\pi}{4} (\alpha f)^2 = 127.97 \text{ mm}^2 \tag{4}$$

For $\lambda = 565$ nm, both limits apply and $C_E = 6.67 \cdot 10^{-3}$; $C_T = 1$; $P = 5.44$; $C_B = 10^{0.02(\lambda-450)}$. The limits are MPE$_T = 47.90$ mW and MPE$_C = 62.54$ mW. Therefore, the limiting factor is MPET which results in 47.90 mW entering the

Table 3 Animal groups.

Ti vs TiN comparison			TiN irradiance threshold		Photovoltaic RF		Pixel switch		Pattern reversal		Contrast sensitivity	
Fig. 4b–f			Fig. 4g, h		Fig. 5		Fig. 6		Figs. 7 and 8		Fig. 9	
Sex	**Age**	**Material**	**Sex**	**Age**	**Sex**	**Age**	**Sex**	**Age**	**Sex**	**Age**	**Sex**	**Age**
Male	133	Ti	Male	115	Female	137	Male	108	Male	122	Male	133
Male	141	Ti	Male	123	Male	117	Male	130	Male	103	Male	131
Male	108	Ti	Female	127	Male	119	Male	108	Male	132		
Female	116	Ti	Female	134	Male	148	Male	108	Male	136		
Female	114	Ti	**Pharmacology**		Male	123			Male	152		
Male	117	Ti	Fig. 4g, h, i, j		Female	127						
Male	142	Ti	Male	115	Female	134						
Male	146	Ti	Male	107	Male	135						
Male	148	Ti	Male	108	Male	138						
Female	142	TiN	Female	147	Male	139						
Male	108	TiN	Female	143								
Female	96	TiN										
Male	119	TiN										
Male	146	TiN										
Male	148	TiN										

Sex and age of the rd10 mice used in the study.

pupil and corresponds to 374.3 µW mm^{-2} for an exposed area of 127.97 mm^2. However, POLYRETINA operates with pulsed illumination. With pulses of 10 ms and a duty cycle of 20%, 10% or 5% (respectively, for 20, 10 or 5 Hz), the MPE is increased to 1.87, 3.74 or 7.48 mW mm^{-2}, respectively[75]. In addition, a previous thermal model showed that at 565 nm and over the broad range of irradiance levels the temperature increase in the retina is reduced by 11% with POLYRETINA[11]. Therefore, the MPE could be increased to 2.08, 4.16 or 8.32 mW mm^{-2}, respectively, for 20, 10 or 5 Hz.

Statistical analysis and graphical representation. Statistical analysis and graphical representation were performed with Prism (GraphPad Software Inc.) and MATLAB. The normality test (D'Agostino & Pearson omnibus normality test) was performed in each dataset to justify the use of a parametric or non-parametric test. In each figure P values were represented as *$P < 0.05$, **$P < 0.01$, ***$P < 0.001$ and ****$P < 0.0001$.

Reporting summary. Further information on research design is available in the Nature Research Reporting Summary linked to this article.

Data availability

The authors declare that all other relevant data supporting the findings of the study are available in this article and in its Supplementary Materials. Access to our raw data can be obtained from the corresponding author upon reasonable request.

References

1. Ghezzi, D. Retinal prostheses: progress toward the next generation implants. *Front. Neurosci.* **9**, 290 (2015).
2. Zrenner, E. Fighting blindness with microelectronics. *Sci. Transl. Med.* **5**, 210ps16–210ps16 (2013).
3. Lewis, P. M., Ackland, H. M., Lowery, A. J. & Rosenfeld, J. V. Restoration of vision in blind individuals using bionic devices: a review with a focus on cortical visual prostheses. *Brain Res.* **1595**, 51–73 (2015).
4. Luo, Y. H.-L. & da Cruz, L. The Argus® II retinal prosthesis system. *Prog. Retin. Eye Res.* **50**, 89–107 (2016).
5. Stingl, K. et al. Artificial vision with wirelessly powered subretinal electronic implant alpha-IMS. *Proc. Biol. Sci.* **280**, 20130077 (2013).
6. Gaillet, V. et al. Spatially selective activation of the visual cortex via intraneural stimulation of the optic nerve. *Nat. Biomed. Eng.* **4**, 181–194 (2020).
7. Veraart, C. et al. Visual sensations produced by optic nerve stimulation using an implanted self-sizing spiral cuff electrode. *Brain Res.* **813**, 181–186 (1998).
8. Normann, R. A., Maynard, E. M., Rousche, P. J. & Warren, D. J. A neural interface for a cortical vision prosthesis. *Vision Res.* **39**, 2577–2587 (1999).
9. Dobelle, W. H., Mladejovsky, M. G., Evans, J. R., Roberts, T. S. & Girvin, J. P. 'Braille' reading by a blind volunteer by visual cortex stimulation. *Nature* **259**, 111–112 (1976).
10. Maya-Vetencourt, J. F. et al. A fully organic retinal prosthesis restores vision in a rat model of degenerative blindness. *Nat. Mater.* **16**, 681–689 (2017).
11. Ferlauto, L. et al. Design and validation of a foldable and photovoltaic wide-field epiretinal prosthesis. *Nat. Commun.* **9**, 992 (2018).
12. Tang, J. et al. Nanowire arrays restore vision in blind mice. *Nat. Commun.* **9**, 786 (2018).
13. Weitz, A. C. et al. Improving the spatial resolution of epiretinal implants by increasing stimulus pulse duration. *Sci. Transl. Med.* **7**, 318ra203–318ra203 (2015).
14. Hamel, C. Retinitis pigmentosa. *Orphanet J. Rare Dis.* **1**, 40 (2006).
15. Dagnelie, G. et al. Performance of real-world functional vision tasks by blind subjects improves after implantation with the Argus® II retinal prosthesis system: Functional vision tasks using Argus® II. *Clin. Exp. Ophthalmol.* **45**, 152–159 (2017).
16. Stingl, K. et al. Subretinal visual implant alpha IMS—clinical trial interim report. *Vision Res.* **111**, 149–160 (2015).
17. Ahuja, A. K. et al. Blind subjects implanted with the Argus II retinal prosthesis are able to improve performance in a spatial-motor task. *Br. J. Ophthalmol.* **95**, 539–543 (2011).
18. Erickson-Davis, C. & Korzybska, H. What do blind people "see" with retinal prostheses? Observations and qualitative reports of epiretinal implant users. *Plos ONE* **16**, e0229189 (2021).
19. Ho, A. C. et al. Long-term results from an epiretinal prosthesis to restore sight to the blind. *Ophthalmology* **122**, 1547–1554 (2015).
20. Dorn, J. D. et al. The detection of motion by blind subjects with the epiretinal 60-electrode (Argus II) retinal prosthesis. *JAMA Ophthalmol.* **131**, 183–189 (2013).
21. Weiland, J. D. & Humayun, M. S. Retinal prosthetic systems for the treatment of blindness. *Bridge* **42**, 51–57 (2012).
22. Hahm, B.-J. et al. Depression and the vision-related quality of life in patients with retinitis pigmentosa. *Br. J. Ophthalmol.* **92**, 650–654 (2008).
23. Perez Fornos, A., Sommerhalder, J., Pittard, A., Safran, A. B. & Pelizzone, M. Simulation of artificial vision: IV. Visual information required to achieve simple pointing and manipulation tasks. *Vision Res.* **48**, 1705–1718 (2008).
24. Sommerhalder, J. & Perez Fornos, A. Prospects and limitations of spatial resolution. in *Artificial Vision* (ed. Gabel, V. P.) 29–45 (Springer International Publishing, 2017).
25. Dagnelie, G. et al. Real and virtual mobility performance in simulated prosthetic vision. *J. Neural Eng.* **4**, S92–S101 (2007).
26. Cha, K., Horch, K. W. & Normann, R. A. Mobility performance with a pixelized vision system. *Vision Res.* **32**, 1367–1372 (1992).
27. Thorn, J. T., Migliorini, E. & Ghezzi, D. Virtual reality simulation of epiretinal stimulation highlights the relevance of the visual angle in prosthetic vision. *J. Neural Eng.* **17**, 056019 (2020).

28. Chen, S. C., Suaning, G. J., Morley, J. W. & Lovell, N. H. Simulating prosthetic vision: II. Measuring functional capacity. *Vision Res.* **49**, 2329–2343 (2009).

29. Beyeler, M., Rokem, A., Boynton, G. M. & Fine, I. Learning to see again: biological constraints on cortical plasticity and the implications for sight restoration technologies. *J. Neural Eng.* **14**, 051003 (2017).

30. Lohmann, T. K. et al. The very large electrode array for retinal stimulation (VLARS)—a concept study. *J. Neural Eng.* **16**, 066031 (2019).

31. Abbott, C. J. et al. Safety studies for a 44-channel suprachoroidal retinal prosthesis: a chronic passive study. *Investig. Ophthalmol. Vis. Sci.* **59**, 1410–1424 (2018).

32. Kitiratschky, V. B. D. et al. Safety evaluation of "retina implant alpha IMS"—a prospective clinical trial. *Graefes. Arch. Clin. Exp. Ophthalmol.* **253**, 381–387 (2015).

33. Yue, L., Weiland, J. D., Roska, B. & Humayun, M. S. Retinal stimulation strategies to restore vision: Fundamentals and systems. *Prog. Retin. Eye Res.* **53**, 21–47 (2016).

34. Palanker, D., Le Mer, Y., Mohand-Said, S., Muqit, M. & Sahel, J. A. Photovoltaic restoration of central vision in atrophic age-related macular degeneration. *Ophthalmology* **127**, 1097–1104 (2020).

35. Zrenner, E. et al. The subretinal implant ALPHA: implantation and functional results. in *Artificial Vision* (ed. Gabel, V. P.) 65–83 (Springer International Publishing, 2017).

36. Humayun, M. S. et al. Interim results from the international trial of second sight's visual prosthesis. *Ophthalmology* **119**, 779–788 (2012).

37. Edwards, T. L. et al. Assessment of the electronic retinal implant alpha AMS in restoring vision to blind patients with end-stage retinitis pigmentosa. *Ophthalmology* **125**, 432–443 (2018).

38. Behrend, M. R., Ahuja, A. K., Humayun, M. S., Chow, R. H. & Weiland, J. D. Resolution of the epiretinal prosthesis is not limited by electrode size. *IEEE Trans. Neural Syst. Rehabil. Eng.* **19**, 436–442 (2011).

39. Tong, W., Meffin, H., Garrett, D. J. & Ibbotson, M. R. Stimulation strategies for improving the resolution of retinal prostheses. *Front. Neurosci.* **14**, 262 (2020).

40. Gargini, C., Terzibasi, E., Mazzoni, F. & Strettoi, E. Retinal organization in the retinal degeneration 10 (rd10) mutant mouse: a morphological and ERG study. *J. Compar. Neurol.* **500**, 222–238 (2007).

41. Pennesi, M. E. et al. Long-term characterization of retinal degeneration in rd1 and rd10 mice using spectral domain optical coherence tomography. *Investig. Ophthalmol. Vis. Sci.* **53**, 4644–4656 (2012).

42. Margolis, D. J. & Detwiler, P. B. Cellular origin of spontaneous ganglion cell spike activity in animal models of retinitis pigmentosa. *J. Ophthalmol.* **2011**, 507037 (2011).

43. Chenais, N. A. L., Leccardi, M. J. I. A. & Ghezzi, D. Capacitive-like photovoltaic epiretinal stimulation enhances and narrows the network-mediated activity of retinal ganglion cells by recruiting the lateral inhibitory network. *J. Neural Eng.* **16**, 066009 (2019).

44. Stasheff, S. F., Shankar, M. & Andrews, M. P. Developmental time course distinguishes changes in spontaneous and light-evoked retinal ganglion cell activity in rd1 and rd10 mice. *J. Neurophysiol.* **105**, 3002–3009 (2011).

45. Chang, B. et al. Two mouse retinal degenerations caused by missense mutations in the β-subunit of rod cGMP phosphodiesterase gene. *Vision Res.* **47**, 624–633 (2007).

46. Prévot, P.-H. et al. Behavioural responses to a photovoltaic subretinal prosthesis implanted in non-human primates. *Nat. Biomed. Eng.* **4**, 172–180 (2020).

47. Green, D. G. & Kapousta-Bruneau, N. V. Evidence that L-AP5 and D,L-AP4 can preferentially block cone signals in the rat retina. *Vis. Neurosci.* **24**, 9–15 (2007).

48. Jensen, R. J. & Rizzo, J. F. Responses of ganglion cells to repetitive electrical stimulation of the retina. *J. Neural Eng.* **4**, S1–S6 (2007).

49. Freeman, D. K. & Fried, S. I. Multiple components of ganglion cell desensitization in response to prosthetic stimulation. *J. Neural Eng.* **8**, 016008 (2011).

50. Chenais, N. A. L., Airaghi Leccardi, M. J. I. & Ghezzi, D. Naturalistic spatiotemporal modulation of epiretinal stimulation increases the response persistence of retinal ganglion cell. *J. Neural Eng.* https://doi.org/10.1088/1741-2552/abcd6f (2020).

51. Lorach, H. et al. Photovoltaic restoration of sight with high visual acuity. *Nat. Med.* **21**, 476–482 (2015).

52. Delori, F. C., Webb, R. H. & Sliney, D. H. Maximum permissible exposures for ocular safety (ANSI 2000), with emphasis on ophthalmic devices. *J. Optical Soc. Am. A* **24**, 1250–1265 (2007).

53. Lee, D. Y., Lorach, H., Huie, P. & Palanker, D. Implantation of modular photovoltaic subretinal prosthesis. *Ophthalmic Surg. Lasers Imaging Retina* **47**, 171–174 (2016).

54. Ghezzi, D. et al. A polymer optoelectronic interface restores light sensitivity in blind rat retinas. *Nat. Photonics* **7**, 400–406 (2013).

55. Gautam, V., Rand, D., Hanein, Y. & Narayan, K. A polymer optoelectronic interface provides visual cues to a blind retina. *Adv. Mater.* **26**, 1751–1756 (2014).

56. Ghezzi, D. et al. A hybrid bioorganic interface for neuronal photoactivation. *Nat. Commun.* **2**, 166 (2011).

57. Antognazza, M. et al. Characterization of a polymer-based, fully organic prosthesis for implantation into the subretinal space of the rat. *Adv. Healthcare Mater.* **5**, 2271–2282 (2016).

58. Feyen, P. et al. Light-evoked hyperpolarization and silencing of neurons by conjugated polymers. *Sci. Rep.* **6**, 22718 (2016).

59. Ronzani, C. et al. High-frequency stimulation of normal and blind mouse retinas using TiO₂ nanotubes. *Adv. Funct. Mater.* **28**, 1804639 (2018).

60. Palanker, D., Vankov, A., Huie, P. & Baccus, S. Design of a high-resolution optoelectronic retinal prosthesis. *J. Neural Eng.* **2**, S105–S120 (2005).

61. Bullimore, M. A., Bailey, I. L. & Wacker, R. T. Face recognition in age-related maculopathy. *Investig. Ophthalmol. Vis. Sci.* **32**, 2020–2029 (1991).

62. Bach, M., Wilke, M., Wilhelm, B., Zrenner, E. & Wilke, R. Basic quantitative assessment of visual performance in patients with very low vision. *Investig. Ophthalmol. Vis. Sci.* **51**, 1255–1260 (2010).

63. Smith, A. T. *Visual Perception: Physiology, Psychology and Ecology* (SAGE Publications Sage UK, 1997).

64. Parush, A., Parush, D. & Ilan, R. Human factors in healthcare: a field guide to continuous improvement. *Synthesis Lectures on Assistive, Rehabilitative, and Health-Preserving Technologies* **6**, i–202 (2017).

65. Dräger, U. C. & Olsen, J. F. Ganglion cell distribution in the retina of the mouse. *Investig. Ophthalmol. Vis. Sci.* **20**, 285–293 (1981).

66. Dhande, O. S. & Huberman, A. D. Visual circuits: mouse retina no longer a level playing field. *Curr. Biol.* **24**, R155–R156 (2014).

67. Baden, T. et al. The functional diversity of retinal ganglion cells in the mouse. *Nature* **529**, 345–350 (2016).

68. Dacey, D. M. & Petersen, M. R. Dendritic field size and morphology of midget and parasol ganglion cells of the human retina. *Proc. Natl Acad. Sci. USA* **89**, 9666–9670 (1992).

69. Dacey, D. M. The mosaic of midget ganglion cells in the human retina. *J. Neurosci.* **13**, 5334–5355 (1993).

70. Peterson, B. B. & Dacey, D. M. Morphology of wide-field, monostratified ganglion cells of the human retina. *Vis. Neurosci.* **16**, 107–120 (1999).

71. Michels, R. G., Wilkinson, C. P. & Rice, T. A. *Retinal Detachment* (The CV Mosby Company, 1990).

72. Nagra, M., Gilmartin, B., Thai, N. J. & Logan, N. S. Determination of retinal surface area. *J. Anat.* **231**, 319–324 (2017).

73. Lee, J.-I. & Im, M. Non-rectangular waveforms are more charge-efficient than rectangular one in eliciting network-mediated responses of ON type retinal ganglion cells. *J. Neural Eng.* **15**, 055004 (2018).

74. Boinagrov, D., Pangratz-Fuehrer, S., Goetz, G. & Palanker, D. Selectivity of direct and network-mediated stimulation of the retinal ganglion cells with epi-, sub- and intraretinal electrodes. *J. Neural Eng.* **11**, 026008 (2014).

75. Airaghi Leccardi, M. J. I. et al. Photovoltaic organic interface for neuronal stimulation in the near-infrared. *Commun. Mater.* **1**, 21 (2020).

76. Simone, G. et al. Near-infrared tandem organic photodiodes for future application in artificial retinal implants. *Adv. Mater.* **30**, 1804678 (2018).

77. Zrenner, E. et al. Subretinal electronic chips allow blind patients to read letters and combine them to words. *Proc. Biol. Sci.* **278**, 1489–1497 (2011).

78. Chuang, A. T., Margo, C. E. & Greenberg, P. B. Retinal implants: a systematic review. *Br. J. Ophthalmol.* **98**, 2013 (2014).

79. Quiroga, R. Q., Nadasdy, Z. & Ben-Shaul, Y. Unsupervised spike detection and sorting with wavelets and superparamagnetic clustering. *Neural Comput.* **16**, 1661–1687 (2004).

80. Tsuchiya, T., Hirata, M. & Chiba, N. Young's modulus, fracture strain, and tensile strength of sputtered titanium thin films. *Thin Solid Films* **484**, 245–250 (2005).

81. Chen, Z. & Diebels, S. Nanoindentation of soft polymers: modeling, experiments and parameter identification. *Technische Mechanik* **34**, 166–189 (2014).

82. Savagatrup, S. et al. Mechanical degradation and stability of organic solar cells: molecular and microstructural determinants. *Energy Environ. Sci.* **8**, 55–80 (2015).

83. Lang, U., Naujoks, N. & Dual, J. Mechanical characterization of PEDOT:PSS thin films. *Synthetic Metals* **159**, 473–479 (2009).

84. Robin, C. J., Vishnoi, A. & Jonnalagadda, K. N. Mechanical behavior and anisotropy of spin-coated SU-8 thin films for MEMS. *J. Microelectromech. Syst.* **23**, 168–180 (2014).

85. Hasenkamp, W. et al. Polyimide/SU-8 catheter-tip MEMS gauge pressure sensor. *Biomed. Microdevices* **14**, 819–828 (2012).

86. Isselé, H. et al. Determination of the Young's Modulus of a TiN thin film by nanoindentation: analytical models and FEM simulation. *e-J. Surf. Sci. Nanotech.* **10**, 624–629 (2012).

87. Hammer, M., Roggan, A., Schweitzer, D. & Müller, G. Optical properties of ocular fundus tissues—an in vitro study using the double-integrating-sphere technique and inverse Monte Carlo simulation. *Phys. Med. Biol* **40**, 963–978 (1995).

88. Narasimhan, A. & Jha, K. Bio-heat transfer simulation of square and circular array of retinal laser irradiation. *Front. Heat Mass Transfer* **2**, 033005 (2011).

89. Sardar, D. K., Yust, B. G., Barrera, F. J., Mimun, L. C. & Tsin, A. T. Optical absorption and scattering of bovine cornea, lens and retina in the visible region. *Lasers Med. Sci.* **24**, 839–847 (2009).

90. Mirnezami, S. A., Rajaei Jafarabadi, M. & Abrishami, M. Temperature distribution simulation of the human eye exposed to laser radiation. *J. Lasers Med. Sci.* **4**, 175–181 (2013).

91. Gosalia, K., Weiland, J., Humayun, M. & Lazzi, G. Thermal elevation in the human eye and head due to the operation of a retinal prosthesis. *IEEE Trans. Biomed. Eng.* **51**, 1469–1477 (2004).

92. Wang, J. et al. Retinal safety of near-infrared lasers in cataract surgery. *J. Biomed. Optics* **17**, 0950011–09500112 (2012).

93. Brown, J. S. et al. In vivo human choroidal thickness measurements: evidence for diurnal fluctuations. *Investig. Ophthalmol. Vis. Sci.* **50**, 5–12 (2009).

Acknowledgements

Author contributions

N.A.L.C. designed, performed and analysed spatial selectivity measurements and electrophysiological experiments and wrote the paper. M.J.I.A.L. designed, fabricated and characterised the prosthesis and performed mechanical and thermal simulations. D.G. designed and led the study, and wrote the paper. All the authors read and accepted the paper.

Competing interests

The authors declare no competing interests.

Additional information

Supplementary information The online version contains supplementary material available at https://doi.org/10.1038/s43246-021-00133-2.

Correspondence and requests for materials should be addressed to D.G.

Peer review information Primary handling editor: John Plummer

Reprints and permission information is available at http://www.nature.com/reprints

Publisher's note Springer Nature remains neutral with regard to jurisdictional claims in published maps and institutional affiliations.